International Journal of Hydrogen Energy 262 (2026) 156713

Contents lists available at ScienceDirect

International Journal of Hydrogen Energy

journal homepage: www.elsevier.com/locate/he

# Toward ultra-low emissions combustion in a dual fuel diesel-hydrogen engine under low load condition: a 3D-CFD study

Alfredo Maria Pisapia [a], Carlo Alberto Rinaldini [a,*], Francesco Scrignoli [a], Xinyan Wang [b], Hua Zhao [b]

[a] Dipartimento di Ingegneria "Enzo Ferrari", Università degli Studi di Modena e Reggio Emilia, via Pietro Vivarelli 10, Modena, 41125, Italy
[b] Centre for Advanced Powertrain and Fuels, Brunel University of London, Uxbridge, London, UB8 3PH, United Kingdom

ARTICLE INFO

*Keywords:*
Hydrogen
3D-CFD simulation
Dual fuel
RCCI
Heavy duty
Injection law optimization

ABSTRACT

Decarbonising Compression Ignition (CI) engines remains critical in marine, heavy-duty and off-road sectors with long asset lifetimes favouring retrofit solutions. Hydrogen can displace Diesel, yet ultra-high Hydrogen Energy Share (HES) is limited by rapid heat release, $NO_x$ formation and excessive pressure rise. This study employs a 3D-CFD model, calibrated against nine experimental operating points, to numerically explore ultra-high HES in a dual fuel Diesel–hydrogen engine at low load (1200 rpm, IMEP = 6 bar). A single-pilot Reactivity Controlled Compression Ignition (RCCI) strategy, with advanced Diesel injection promoting distributed ignition of an ultra-lean $H_2$–air mixture, extends hydrogen utilization without violating mechanical or emissions constraints. Two configurations emerge: HES = 96% (SOI = 660°CA) delivers +4.4% gross indicated efficiency, −88.6% $CO_2$ and −98% $NO_x$; HES = 98% (SOI = 655°CA) achieves −94% $CO_2$ and −99.7% $NO_x$. In both cases the peak in-cylinder pressure and the Peak Pressure Rise Rate stay within the structural design limits of the single-cylinder research engine used in this study (180 bar and 20 bar/°CA respectively).

Nomenclature

| | |
|---|---|
| Abbreviations and Acronyms | |
| 2IVO | Second Intake Valve Opening |
| 3D-CFD | Three-Dimensional Computational Fluid Dynamics |
| AFTDC | After Firing Top Dead Center |
| AHRR | Apparent Heat Release Rate (J/deg) |
| CA | Crank Angle |
| CA10–90 | turbulent combustion duration (deg) |
| CI | Compression Ignition |
| CR | Compression Ratio (−) |
| DF | Dual Fuel |
| DOE | Design Of Experiment |
| ECFM-3Z | Extended Coherent Flame Model – Three Zones |
| EGR | Exhaust Gas Recirculation |
| EVO | Exhaust Valve Olosing |
| GIE | Gross Indicated Efficiency (%) |
| HCCI | Homogeneous Charge Compression Ignition |
| HD | Heavy Duty |
| HES | Hydrogen Energy Share (−) |
| ICE | Internal Combustion Engine |
| iEGR | internal EGR |
| IMEP | Indicated Mean Effective Pressure (bar) |

(continued on next column)

(continued)

| | |
|---|---|
| IMEP* | gross Indicated Mean Effective Pressure (bar) |
| IVC | Intake Valve Closing |
| LHV | Lower Heating Value (MJ/kg) |
| LHV* | relative Lower Heating Value (MJ/kg) |
| LIVC | Late Intake Valve Closing |
| PFI | Port Fuel Injection |
| $P_{max}$ | Peak in-cylinder pressure (bar) |
| PPRR | Peak Pressure Rise Rate (bar/deg) |
| RCCI | Reactivity Controlled Compression Ignition |
| SOI | Start Of Injection |
| TDC | Top Dead Center |
| VVA | Variable Valve Actuation |
| **Chemical formulae** | |
| $C_7H_{16}$ | n-heptane |
| CO | carbon monoxide |
| $CO_2$ | carbon dioxide |
| $H_2$ | hydrogen |
| $NO_x$ | nitrogen oxides |
| **Symbols and Units** | |
| k | specific heat ratio |
| $\alpha_{st}$ | stoichiometric air-fuel ratio |
| $\eta_c$ | combustion efficiency |

(continued on next page)

* Corresponding author.
*E-mail address:* carloalberto.rinaldini@unimore.it (C.A. Rinaldini).

https://doi.org/10.1016/j.ijhydene.2026.156713
Received 12 March 2026; Received in revised form 17 July 2026; Accepted 19 July 2026
Available online 31 July 2026

(*continued*)

| | |
|---|---|
| $\lambda_g$ | global excess air ratio |
| $\lambda_{H2}$ | $H_2$–air excess air ratio |
| $\lambda_v$ | volumetric efficiency |

## 1. Introduction

Climate change mitigation requires rapid and sustained reductions in greenhouse-gas emissions across all energy-intensive sectors [1–4]. This imperative extends to Heavy-Duty (HD) road transport, off-road machinery and marine propulsion, where decarbonisation remains particularly challenging in the near term because of demanding duty cycles, long asset lifetimes and stringent reliability requirements [5–7]. Compression Ignition (CI) engines therefore continue to be a cornerstone technology in these applications, supported by a large installed base expected to persist for years, which motivates retrofit-oriented solutions that lower lifecycle carbon intensity while preserving efficiency and robustness [8–10].

Among alternative energy carriers, hydrogen ($H_2$) is attractive because it contains no carbon at the point of use and can be produced via low-carbon pathways. Accordingly, $H_2$–Diesel Dual Fuel (DF) concepts have received increasing attention as a transitional route to reduce $CO_2$ emissions without abandoning CI architectures [11–14]. In a typical DF strategy, $H_2$ is supplied as a premixed or partially premixed fuel (e.g., intake addition [15–17]), while a small quantity of Diesel is directly injected to ensure reliable auto-ignition and maintain combustion controllability; this enables a progressive displacement of Diesel energy and, in many cases, a reduction in soot owing to the absence of carbon in $H_2$ [18,19]. Consistent with this rationale, Saravanan and Nagarajan [20] experimentally showed that port-injected $H_2$ can markedly reduce smoke across the load range, while also revealing a tendency for $NO_x$ to rise at high load and for knock to emerge at the highest $H_2$ flow rates, thereby highlighting both the emissions benefit and the practical combustion constraints of DF operation. More generally, the achievable Hydrogen Energy Share (HES), defined as the fraction of the total fuel energy (based on lower heating value) provided by $H_2$, is bounded by coupled limits involving combustion phasing, emissions and engine mechanical loading [20]. Chintala and Subramanian [21] reported that the maximum attainable HES at full load was knock-limited and coincided with the admissible peak in-cylinder pressure in the baseline high-compression configuration. The same study identified Compression Ratio (CR) as an additional boundary condition, with reduced CR markedly relaxing knock and peak-pressure limitations and enabling substantially higher knock-limited HES. From a mechanistic standpoint, the fast burning of $H_2$ steepens the heat-release profile, elevating the Peak Pressure Rise Rate (PPRR) and the peak in-cylinder pressure (Pmax) [22], while high local temperatures and non-uniform combustion promote $NO_x$ formation, especially at high load [23–25]; conversely, dilution strategies often required to contain $NO_x$ and PPRR may penalise charge reactivity and combustion stability at low load [26]. Within this multi-constraint space, the Diesel injection strategy represents a primary control lever: whereas conventional late-injection schemes generate Diesel-rich pockets that burn in diffusion-controlled, high-temperature regions, markedly advanced pilot-oriented strategies increase premixing time and promote an HCCI-like (homogeneous or partially premixed) combustion of the Diesel fraction. In such a Reactivity Controlled Compression Ignition (RCCI) framework, Diesel acts as a distributed auto-ignition source for the ultra-lean $H_2$–air charge [27–29]. Because these phenomena are governed by local in-cylinder air-to-fuel ratio, turbulence and temperature stratification, Three-Dimensional Computational Fluid Dynamics (3D-CFD) is a valuable tool for DF combustion development; however, its predictive capability requires careful calibration and validation against experiments under representative DF conditions.

Accordingly, an established 3D-CFD approach was applied to a single-cylinder, large-displacement research engine converted to operate in DF Diesel–$H_2$ mode (DF D-$H_2$). The experimental platform adopts a Miller-cycle strategy via Late Intake Valve Closing (LIVC), reducing the effective compression ratio and providing an additional safety margin against excessive pressure rise and abnormal combustion during high-HES operations [21]. The 3D-CFD model was first calibrated and validated against experiments across nine operating points, and the resulting setup was then used to investigate and optimize the Diesel injection strategy under a representative DF low-load condition (1200 rpm, Indicated Mean Effective Pressure (IMEP) = 6 bar).

As summarized in Table 1, although the entire HES range has been explored across a variety of CI engine architectures and operating conditions, ultra-high HES values are almost exclusively reported at low load; at higher loads, reaching the upper HES range typically requires additional control levers such as Exhaust Gas Recirculation (EGR), water injection or compression-ratio reduction. Among the few experimental investigations approaching the upper bound, Rameez and Mohamed Ibrahim [32] recently obtained 90% HES at 2 bar BMEP through a dual-pulse Diesel injection in an RCCI arrangement. Dimitriou et al. [33] attained 98% HES at low load on a HD multi-cylinder engine in EGR-off conditions, through a single Diesel pre-injection at conventional timing (−24°CA BTDC) in a conventional DF framework. Despite this body of experimental evidence, it has not yet been demonstrated whether a single, markedly advanced Diesel pilot, without recourse to dual-pulse injection, EGR or water injection, can sustain an RCCI regime up to HES values approaching 99%.

The main aim of the present work is therefore to numerically investigate, through an experimentally calibrated 3D-CFD framework, the feasibility of ultra-high HES (≥96%) Diesel–$H_2$ DF operation under representative low-load conditions, by reorienting the Diesel injection strategy from a conventional pilot–main pattern toward a single, markedly advanced Diesel pilot promoting an RCCI regime. The study is conceived as a conceptual numerical demonstration at low load, intended to delineate the achievable combustion behaviour and the associated mechanical and emission trade-offs, and to guide future experimental validation activities at extreme HES values.

Building on recent experimental investigations of $H_2$–Diesel RCCI combustion (Table 1), the novelty of the present study lies in three contributions.

- The calibration of a 3D-CFD model on a comprehensive nine-point experimental dataset spanning three loads (IMEP = 6, 12 and 18 bar) and three global excess-air ratios, providing a robust numerical setup for DF Diesel–$H_2$ combustion in a HD CI architecture;
- The numerical demonstration that a single, markedly advanced Diesel pilot, without recourse to dual-pulse injection, EGR or water injection, can drive an RCCI regime extending the HES up to 98% at partial load, while keeping the PPRR within the engine mechanical limit;
- The quantitative benchmarking of the resulting $NO_x$ emissions against the Euro 7 thresholds for on-road HD engines.

Results show that, under the investigated operating condition (1200 rpm, IMEP = 6 bar), the proposed approach enables HES values up to 98% while preserving the Gross Indicated Efficiency (GIE), containing Pmax and PPRR within the engine mechanical envelope, and substantially reducing both carbon-based emissions and $NO_x$ with respect to the baseline configuration. By systematically linking injection timing, combustion characteristics and mechanical constraints, the present study provides a numerical pathway toward ultra-high $H_2$ substitution in HD CI engines, supporting future experimental validation activities.

**Table 1**
Overview of representative Diesel–$H_2$ dual-fuel studies, ordered by increasing maximum HES.

| Reference | Approach | Engine class | Speed | Load condition | $H_2$ supply | Combustion strategy | Max HES |
|---|---|---|---|---|---|---|---|
| Gregory K. Lilik et al. (2010) [23] | Exp, Num. | MC*, DI Diesel engine | 1800/ 3600 rpm | Low, mid high loads | Fumigation | Conventional DF combustion | 15% |
| Saravanan & Nagarajan (2009) [30] | Exp | SC**, DI, Diesel engine | 1500 rpm | Low to high loads | PFI | Conventional DF combustion | 24.4% |
| Talibi et al. (2017) [26] | Exp | SC**, DI, Diesel engine | 1200 rpm | Mid, high load | PFI | Conventional DF combustion | 41% |
| V. Chintala et al. (2017) [21] | Exp, Num | SC**, DI Diesel Engine | 1500 rpm | Mid and High load | PFI | Conventional DF combustion with water injection at high load | 60% @high load with water |
| Tomita et al. (2001) [31] | Exp | SC**, DI, Diesel engine | 1000 rpm | Low, mid-low loads | PFI | - | 80% |
| P. V. Rameez et al. (2024) [32] | Exp | MC*, DI, Diesel engine | 1800 rpm | Low load | PFI | Conventional DF and RCCI combustion | 90% |
| Pavlos Dimitriou et al. (2018) [33] | Exp | MC*, DI Diesel engine | 1500 rpm | Low and mid loads | PFI | Conventional DF combustion, EGR-off | 98% @ low load |

MC* Multi Cylinder, SC** Single Cylinder.

## 2. Methodology

The present study combines 3D-CFD simulations with experimental data acquired on a single-cylinder HD research engine operating in DF D-$H_2$ mode. The methodology was organised in two main steps.

- Development and calibration of a detailed 3D-CFD combustion and emissions model against dedicated test-bench measurements over nine operating points, obtained by combining three loads (IMEP = 6, 12 and 18 bar) with three global air–fuel ratios at each load, at a fixed engine speed of 1200 rpm.
- Optimization of the Diesel injection strategy to enable ultra-high HES under low-load conditions (IMEP = 6 bar).

The calibration phase ensured that the numerical framework could reproduce the main combustion and emissions trends over a representative portion of the engine map. The subsequent optimization campaign was carried out at low load, where structural constraints are less restrictive. In particular, the injection strategy analysis focused on a single representative DF operating point at IMEP = 6 bar and global excess-air ratio $\lambda_g = 2.56$, which was used as the reference configuration for all the parametric variations in Diesel injection optimization. At this operating point, a Design Of Experiments (DOE) was defined by selecting discrete target HES levels and sweeping the Start Of Injection (SOI) of a single Diesel injection over a wide crank angle window, while keeping all the other engine operating parameters fixed. This approach effectively isolated the impact of HES on the combustion characteristics and emission formation and was justified by the capability of the external boosting system to restore the volumetric efficiency ($\lambda_v$) losses induced by higher $H_2$ concentrations at the intake, thereby ensuring experimental repeatability of the operating conditions analysed in this numerical study.

The primary objective of the DOE was to act on the injection law of the high reactivity fuel to drastically reduce fossil fuel utilization and, hence, $CO_2$ emissions, while controlling $NO_x$ formation. Previous experimental and numerical works showed that, although $H_2$ substitution can improve efficiency and lower carbon-based emissions, $NO_x$ emissions tend to increase with increasing injected $H_2$ due to faster heat-release rates and higher combustion temperatures [21]. Starting from the baseline low load condition, by systematically adjusting both Diesel quantity and SOI, the analysis pushed previous DF D-$H_2$ investigations [34–36] towards their practical physical limits in terms of achievable HES. The specific goals were to identify injection strategies that minimize Diesel demand and $CO_2$ emissions, maintain combustion stability and acceptable mechanical loads, and achieve a substantial reduction of $NO_x$.

Since no coupled 0D/1D model was employed to provide boundary conditions to the 3D domain, the numerical analysis was restricted to the closed-valve portion of the cycle. Therefore, only the cylinder volume was modelled, whereas intake and exhaust ports and manifolds were neglected. The in-cylinder thermodynamic state and flow field at Intake Valve Closing (IVC) were reconstructed from experimental data. This procedure ensured consistency between the test-bench conditions and the initial conditions of the simulations. Overall, this approach concentrated the computational effort on the in-cylinder processes that most directly govern Diesel-air mixture formation, ignition, combustion and pollutant formation, while keeping the computational costs of the injection-optimization study manageable.

### 2.1. Engine setup

The experimental and numerical activities were carried out based on a single-cylinder research engine derived from the Yuchai YC6K six-cylinder HD Diesel engine at the Centre of Advanced Powertrain and Fuels at Brunel University of London to operate in DF condition. The short block and crankcase assembly were entirely re-engineered by AVL, featuring two counter-rotating balance shafts to minimize mechanical vibrations and ensure smooth operation in steady and transient conditions. This configuration was developed to reproduce the thermodynamic behaviour of a large-bore commercial engine under fully controlled laboratory conditions, enabling flexible operation with both conventional and alternative fuels. The engine's main specifications are reported in Table 2.

The VVA system, developed by Jacobs Vehicle Systems, relies on a

**Table 2**
Single cylinder engine specification.

| Engine parameter | Description |
|---|---|
| Bore × Stroke (mm × mm) | 129 × 155 |
| Cylinder displacement (cc) | 2026 |
| Connecting rod length (mm) | 256 |
| Geometric compression ratio | 16.8 |
| Max. in-cylinder pressure (bar) | 180 |
| Max. PPRR (bar/deg) | 20 |
| Max. engine speed (rpm) | 1900 |
| Bowl shape | Re-entrant Diesel bowl |
| N. of valves | 4 |
| Intake/Exhaust valve diameter (mm/mm) | 43.9/40.4 |
| Intake cam opening/closing (° CA ATDC) | Variable |
| Max. intake valve lift (mm) | Variable |
| Exhaust cam opening/closing (°CA ATDC) | 144/360 (at 0.5 mm valve lift) |
| Max. exh. valve lift (mm) | 14 |
| Diesel injector | Bosch CRIN 3.22 central DI injector; 8-hole nozzle, 150° spray angle; hole diameter 0.176 mm; common-rail system; max rail pressure 2200 bar |

lost-motion hydraulic mechanism that decouples the valve motion from the fixed cam profile. A high-pressure oil circuit, controlled by an electro-hydraulic solenoid valve, regulates the oil flow to the lost-motion chamber, thereby adjusting the effective intake valve timing and duration independently of the camshaft rotation. A schematic view of the solenoid assembly is depicted in Fig. 1. This configuration allows real-time modulation of the IVC, making it possible to reproduce both Late Intake Valve Closing (LIVC) and the Second Intake Valve Opening (2IVO, [38]), which introduces a brief secondary opening of the intake valve during the exhaust stroke acting as a controllable internal Exhaust Gas Recirculation (iEGR). By delaying the intake valve closure through LIVC, instead, the effective CR decreases while maintaining the expansion ratio constant. In this work, the same Miller-type intake valve lift profile was adopted for all the investigated conditions; the corresponding profile, shown in Fig. 2, clearly highlights the simultaneous application of both 2IVO and LIVC to the intake-valve law.

Valve lift was monitored using a MicroStrain S-DVRT-8 displacement transducer. The exhaust valve train retained a conventional fixed cam profile, with an opening duration of approximately 216°CA and a maximum lift of about 14 mm.

The engine was coupled to an eddy-current dynamometer (Froude Hofmann AG150) capable of both torque and speed control. The Diesel fuel circuit was based on a Bosch CRIN 3.22 common-rail injection system, featuring a centrally located eight-hole injector with 0.176 mm nozzle diameter. Injection pressure was provided by a Bosch CP4–S2 high-pressure pump, capable of delivering up to 2200 bar, and was managed by a Bosch CR.8 electronic control unit (ECU). The system enabled fully independent control of injection pressure, injection timing, and mass split between pilot and main injections, allowing flexible operation from conventional Diesel combustion to advanced DF strategies.

Fuel mass flow in both the supply and return lines was measured through Coriolis mass flow meters (Endress + Hauser Promass 83A), ensuring accurate instantaneous consumption and heat-release estimation. The high-pressure lines and common-rail accumulator were thermally insulated and equipped with pressure sensors for safety and repeatability.

The air path employed a closed-loop external boosting system designed to maintain the desired intake pressure throughout the operating range. A variable-speed electrically driven compressor supplied the intake charge, while a water-cooled intercooler regulated the intake air temperature. Both pressure and temperature sensors (PT100 and piezo-resistive transducers) were installed upstream and downstream of the plenum to ensure accurate boundary control.

The in-cylinder pressure was acquired by means of a piezoelectric pressure transducer with a crank-angle resolution of 0.25°CA; the pressure traces used as a reference for the calibration of the 3D-CFD model were obtained by ensemble-averaging 100 consecutive engine cycles to filter out cycle-to-cycle variability.

The experimental setup was also equipped with a high-pressure cooled Exhaust Gas Recirculation (EGR) loop, which allowed the introduction of recirculated exhaust gases when required. However, it is important to note that for all the operating points analysed in this work,

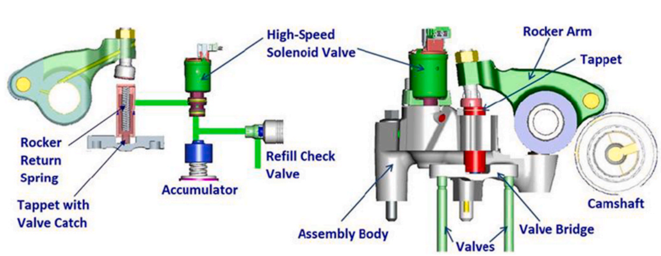


**Fig. 1.** Lost motion intake VVA system with collapsing tappet on the valve side of the rocker arm [37].

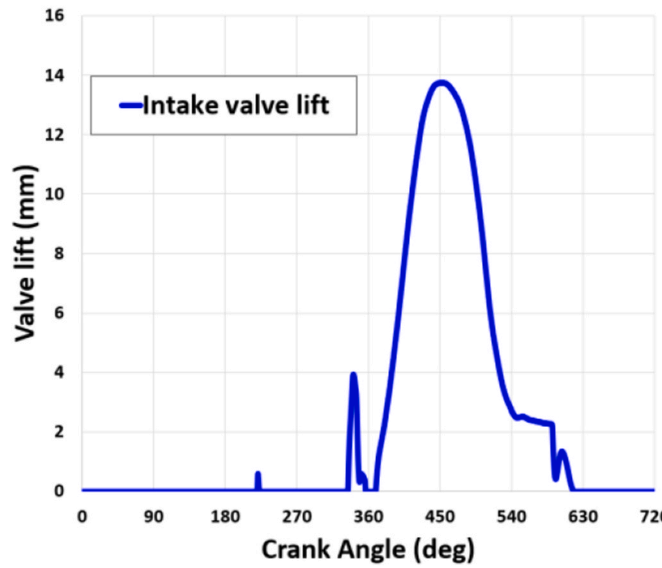


**Fig. 2.** Experimental intake valve lift. This profile is a reference for the CFD simulations.

the EGR system was deactivated, in order to isolate the effects of $H_2$ substitution and Diesel injection strategy on combustion behaviour and emissions. This configuration ensured stable and repeatable intake conditions, providing a well-controlled environment for the calibration and validation of the 3D-CFD model under DF operation.

A simplified schematic of the engine and the main auxiliary units employed during the experimental campaign is shown in Fig. 3. The complete list of the measurement instrumentation, together with the corresponding ranges and accuracies, is reported in Table A.1 (Appendix A). The experimental data acquired in this campaign formed the starting point and a robust basis for the calibration of the 3D-CFD model and for the optimization of the Diesel injection law discussed in the following sections.

It is finally worth commenting on the $H_2$ supply strategy adopted in the present work. $H_2$ was introduced by Port Fuel Injection (PFI), which is the configuration of the experimental platform used for the model calibration (Fig. 3). In recent years, Direct Injection (DI) of $H_2$ has attracted increasing attention, as it can mitigate the $\lambda_v$ penalty associated with the low density of gaseous $H_2$, improve the control of the in-cylinder charge and reduce the risk of backfire and pre-ignition in the intake system. These advantages make DI a promising option, particularly at high load and for high-$H_2$-fraction operation. In the present study, however, PFI was retained because it is representative of low-cost, retrofit-oriented conversions of existing CI engines, which require minimal modifications to the cylinder head and fuel system and are therefore consistent with the transitional decarbonisation scenario targeted by this work. A detailed comparison between PFI and DI $H_2$ supply, including its impact on mixture formation and on the attainable HES, is beyond the scope of the present numerical study and represents an interesting direction for future investigations.

As shown in Fig. 3, The engine-out emissions (namely $NO_x$, CO, $CO_2$, THC, $CH_4$, and $O_2$) as well as the estimated eEGR rate, were monitored using a Horiba MEXA 7170-DEGR emissions analyser. In addition, engine-out soot emissions were assessed using an AVL Smoke Meter 415SE. The concentration of unburned $H_2$ was determined using a VF HSense emissions analyser.

### 2.2. 3D-CFD model

The numerical analysis was structured as a two-step process. First, a calibration phase of the combustion model was carried out under

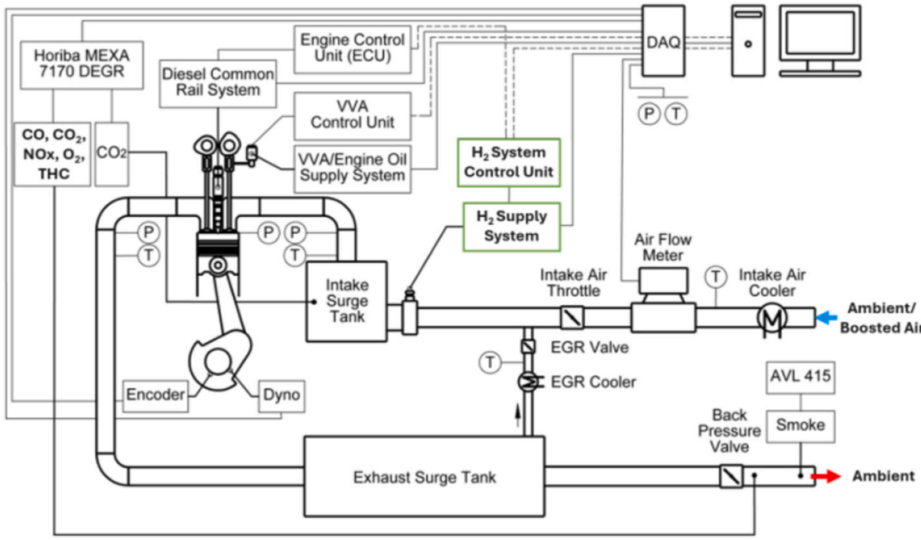


**Fig. 3.** Schematic of the experimental layout and the main auxiliary units employed during the experimental campaign.

baseline DF operating conditions. Second, the calibrated setup was employed to investigate and optimize the Diesel injection strategy with the aim of increasing $H_2$ utilization and HES while maintaining comparable efficiency, reducing emissions and keeping the engine stress below the mechanical limits.

The 3D-CFD simulations were performed using AVL FIRE M [39], widely employed in the automotive industry for both cold non-reactive flows and combustion in internal-combustion engines (ICEs). Since no 0D/1D gas-dynamics model was available to provide crank-angle-resolved boundary conditions accounting for the pressure-wave dynamics of the intake and exhaust systems, including the runners in the 3D domain would have required additional assumptions on the instantaneous boundary pressure and temperature, adding uncertainty and computational cost. The runners were therefore excluded and the analysis was focused on the in-cylinder processes, with the computational domain covering the closed-valve interval from IVC to Exhaust Valve Opening (EVO). This approach is widely adopted for combustion studies in which the interest lies in in-cylinder phenomena (Diesel injection, mixture formation, combustion and emissions) rather than in the detailed gas dynamics of the intake and exhaust systems [40–42]. A direct consequence is that the gas-exchange process is not simulated and the in-cylinder state at IVC is prescribed from the experimental data rather than predicted, consistently with the present focus.

At IVC the in-cylinder charge, composed of $H_2$ and air, was initialized as spatially homogeneous in pressure, temperature and composition, superimposed on a swirl motion consistent with the corresponding experimental condition; pressure and temperature were set so as to reproduce both the measured IVC pressure and the total trapped mass. The homogeneous-mixture assumption is justified by the port-fuel injection of $H_2$, which is introduced far upstream and has ample time and turbulence to mix with the incoming air before IVC. Wall temperatures for the piston crown, liner, head and valves were assigned from literature values for comparable conditions and kept constant over the simulated interval. Because the runners are excluded, pressure-wave dynamics and the associated cycle-to-cycle variability are not captured; these simplifications do not affect the relative comparison between the baseline and the optimized cases but they may affect the absolute reproduction of gas-exchange-dependent quantities, such as the residual-gas content and the cyclic dispersion, which are beyond the scope of the present analysis.

The combustion chamber geometry was derived from a high-fidelity CAD model of the engine (Fig. 4). Special care was devoted to the

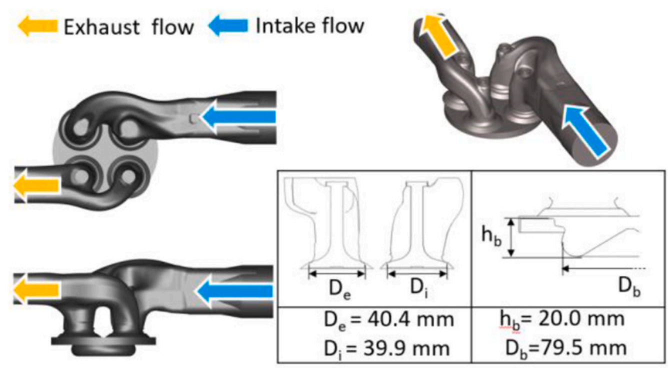


**Fig. 4.** CAD model of the engine, showing the cylinder, the intake and exhaust runners. The direction of the flow is highlighted in the top, side and perspective views. Details of the piston-bowl geometry and intake valves are also reported. Only the in-cylinder region is included in the 3D-CFD domain, while the runners are neglected.

representation of the crevice volumes. The gap between the piston top land and the cylinder liner was explicitly modelled, also capturing the distance between the piston crown and the first piston ring, as well as the crevices associated with the valve seats. Under DF D-$H_2$ operation, these small volumes are particularly relevant, since a fraction of the $H_2$–air mixture can be trapped in these regions and only partially participate in the combustion process, thereby influencing the global combustion efficiency. The availability of a detailed CAD description thus lends robustness to the numerical analysis and allows the 3D-CFD model to reproduce the actual combustion chamber boundaries of the tested engine with high fidelity, ensuring consistency in terms of in-cylinder conditions between simulations and experimental tests.

The simulations were based on the Reynolds-Averaged Navier–-Stokes (RANS) equations, adopting the k–ζ–f turbulence model as closure [43,44]. Spray breakup of Diesel fuel was described by the Kelvin–Helmholtz/Rayleigh–Taylor (KH–RT) breakup model [45,46]. Diesel was represented in the gas-phase reactions by n-heptane ($C_7H_{16}$), which offers a good compromise in terms of chemical fidelity and combustion properties when compared with the fuel employed in the experimental campaign.

In the present study, the k–ζ–f turbulence model, which builds on Durbin's elliptic-relaxation concept [44], was preferred to the more common k–ε closure. Unlike the standard k–ε model, formulated for free-shear, high-Reynolds-number external flows and less accurate near walls and under strong pressure gradients, the k–ζ–f model is specifically tailored to the confined, swirling and highly transient flows of internal-combustion engines, and has been validated for IC-engine applications within the adopted AVL FIRE environment [47,48], consistently with the hybrid wall treatment used here.

Combustion was modelled with the Extended Coherent Flame Model – Three zones (ECFM-3Z model), capable of capturing both premixed and diffusion-controlled combustion regimes. The model resolves three distinct zones (fresh gases, burning mixture and burnt gases) and explicitly accounts for the specific local mixture of the cell [49]. It was coupled with AVL's laminar flame-speed and auto-ignition delay databases, enabling an accurate and reliable prediction of the DF D-$H_2$ combustion process based on experimental data.

The emission sub-models accounted for CO, $CO_2$ and $NO_x$ formation. CO and $CO_2$ were predicted through a two-step global oxidation mechanism, describing the partial oxidation of the surrogate fuel to CO and its subsequent conversion to $CO_2$ (see reaction (1), (2), [39]). In those cells where lean condition is detected, reaction (2) is neglected. This is expected to happen because of the globally lean conditions investigated here. $NO_x$ formation was modelled using the widely recognized extended Zeldovich thermal mechanism [50].

A summary of the physical and chemical sub-models adopted in this work is reported in Table 3, consistently with those described in the previous chapters.

$$C_nH_mO_l + \left(n + \frac{m}{4} - \frac{l}{2}\right)O_2 \rightarrow nCO_2 + \frac{m}{2}\,H_2O \tag{1}$$

$$C_nH_mO_l + \left(\frac{n}{2} - \frac{l}{2}\right)O_2 \rightarrow nCO + \frac{m}{2}\,H_2 \tag{2}$$

where n, m and l represent the number of carbon, hydrogen and oxygen atoms of the considered fuel surrogate.

It is worth clarifying the rationale behind the choice of the ECFM-3Z combustion model and its expected predictive capability for DF Diesel–$H_2$ combustion. The ECFM-3Z model [49] is a three-zone phenomenological flamelet model: rather than solving detailed chemical kinetics in every computational cell, as is the case for fully kinetic-coupled approaches such as the SAGE solver [51], it describes the turbulent combustion through a flame-surface-density transport equation and a local subdivision of each cell into unmixed-fuel, mixed and unmixed-air zones. This formulation allows both premixed and diffusion-controlled regimes to be captured at a substantially lower computational cost than detailed-chemistry approaches, which is a decisive advantage when, as in the present work, a wide nine-point calibration matrix and an extensive injection-strategy DOE must be simulated. The main limitation of a phenomenological model is that it does not resolve the detailed intermediate-species chemistry, so that the absolute prediction of kinetically-controlled quantities is intrinsically less accurate than with detailed-chemistry solvers. In the present setup, however, the most sensitive kinetic features of the DF process are extracted from the AVL tabulated databases of auto-ignition delay times and laminar flame speeds for the Diesel-surrogate/$H_2$/air mixture, which are derived from detailed chemical-kinetic computations and experimental data. This coupling significantly enhances the fidelity of the ECFM-3Z predictions for the ultra-lean $H_2$ combustion regime of interest. Consistently with this modelling choice, $NO_x$ formation is not obtained from a detailed kinetic mechanism but is computed in post-processing through the extended Zeldovich thermal mechanism [50], which is the dominant $NO_x$ pathway under the high-temperature, lean conditions investigated here.

**Table 3**
Main models used for 3D-CFD modelling.

| Equation of State | Real Gas/Peng-Robinson |
|---|---|
| Turbulence model | k-zeta-f |
| Turbulence wall treatment | Hybrid |
| Wall heat transfer model | Standard |
| Breakup model | KH-RT |
| Liquid-Gas drag law | Schiller Naumann |
| Fuel Evaporation model | Dukowicz |
| Diesel surrogate (gas phase) | $C_7H_{16}$ |
| Combustion model | AVL ECFM-3Z |
| Autoignition model | Two-Stage |
| Laminar flame speed | AVL database |
| Auto ignition delay | AVL database |
| $NO_x$ formation model | Thermal (Zeldovich) |

The mesh was generated using AVL FAME M and was entirely composed of polyhedral cells. This choice provides a good compromise between cell count and computational cost, while offering improved robustness in complex geometries compared with purely hexahedral meshes. In particular, polyhedral cells are less prone to severe distortion and "squeezing" in very narrow regions of the domain, such as crevice volumes and valve seat zones, thereby helping to maintain acceptable mesh quality throughout the piston motion.

Starting from this topology, a base cell size of 3 mm was adopted in the bulk of the cylinder volume. To properly resolve the near-nozzle region, two nested conical refinement zones were applied for each injector hole, with characteristic cell sizes of 0.4 mm and 0.2 mm, the finer level being fully embedded within the coarser one. These refinements ensured an adequate description of droplet break-up and vapour–air mixing in the spray development region.

During the combustion phase, an additional volume refinement was activated inside the chamber, reducing the local cell size to 1 mm between −20 and + 40°CA AFTDC (After Firing Top Dead Center). This strategy improved the spatial resolution of flame propagation and local mixture gradients in the main heat-release interval, without excessively increasing the overall cell count in the less critical phases of the cycle (see Fig. 5).

At Top Dead Center (TDC), the resulting mesh comprised approximately $1.13 \times 10^6$ cells (Table 4). This mesh density is consistent with the values typically adopted by the Authors for HD CI and DF engine simulations within the AVL FIRE M framework, and falls within the range recommended by the software guidelines for the prediction of in-cylinder pressure, AHRR and emissions in this engine class.

The timings of the refinement regions within the cylinder volume were adapted to the specific injection strategy under investigation. Different meshes were therefore generated for the various injection laws, all sharing the same nominal mesh parameters (base cell size, refinement levels, boundary-layer resolution) but differing in the activation of the refinements. In this way, the highest spatial resolution was always provided where and when it was most needed, namely during injection and combustion processes.

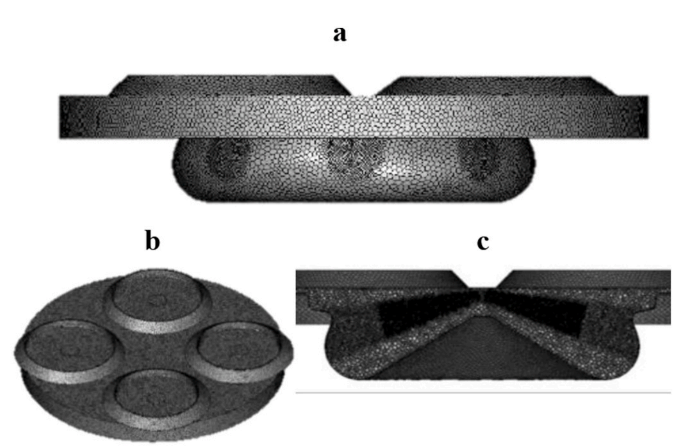


**Fig. 5.** Side (a), perspective (b) and section (c) views of the computational grid at TDC.

**Table 4**
Computational grid details.

| Property | Value |
|---|---|
| Target cell size (mm) | 3 |
| 1st and 2nd injection refinements (mm) | 0.4 and 0.2 |
| Cylinder volume cell size (mm) | 3 (1 from −20 to +40°CA AFTDC) |
| Boundary layer thickness (mm)/n. of layers | 0.1/2 |
| Number of cells @ TDC | 1,130,000 |

From the temporal-discretization standpoint, the time step was chosen based on the authors' experience with similar engine calculations, with the objective of maintaining the Courant–Friedrichs–Lewy (CFL) number below unity throughout the simulated crank angle interval. A coarser crank angle step of 0.5°CA was adopted during the compression stroke, when no strongly transient phenomena occur apart from the evolution of the swirl motion. During the more critical processes of Diesel injection and combustion, the time step was refined to 0.2°CA to cope with the higher velocities of the injected liquid fuel and to adequately resolve both spray dynamics and the rapid propagation of the premixed $H_2$ flame front.

### 2.3. Experimental validation of the DF 3D-CFD model

The calibration of the 3D-CFD combustion model was carried out on a total of nine operating points, covering three engine loads at the same engine speed and three air–fuel ratios for each load condition. For each case (low, medium, and high load), the boost pressure was adjusted to obtain three distinct $\lambda_g$ and the corresponding $H_2$–air excess-air ratios, ($\lambda_{H2}$), while maintaining the same engine speed and injected mass of both fuels. The main parameters characterizing these operating points are summarized in Table 5, which reports engine load, injected Diesel and $H_2$ mass, HES, the adopted injection strategies and other relevant parameters.

The comparison between experiments and simulations was first carried out in terms of in-cylinder pressure trace and Apparent Heat Release Rate (AHRR). For each operating point, AHRR was derived from the measured and simulated pressure traces by applying the first law of thermodynamics (equation (3)), assuming negligible blow-by between piston rings and liner and a constant specific heat coefficient ratio $k = 1.4$. This procedure was applied consistently to both experimental and CFD data, ensuring a coherent evaluation of AHRR across all cases. The resulting pressure and AHRR traces for all nine operating points are shown in Fig. 6, grouped by load level and $\lambda_g$.

The validation was then extended to additional combustion and performance indicators, namely $P_{max}$, PPRR, the combustion phasing parameters CA10, CA50 and CA90, defined as the crank angles at which 10%, 50% and 90% of the total cumulative heat release are attained, and the gross Indicated Mean Effective Pressure (IMEP*; defined in equation (4)). The corresponding results, together with other relevant markers and the associated absolute errors between experiments and simulations, are summarized in three tables (Table 7, Tables 8 and 9), one for each load level.

The initial in-cylinder conditions imposed in the simulations for the nine calibration points are summarized in Table 6, together with the wall temperatures adopted as thermal boundary conditions. For each operating point, the pressure at IVC is taken from the experimental measurement, while the IVC temperature is adjusted to match the experimentally measured trapped mass through the ideal-gas law; the wall temperatures (piston, liner, cylinder head, intake and exhaust valves) are kept constant throughout the simulated cycle at values representative of HD CI engines [52].

Overall, the calibration confirms a satisfactory match between experiments and simulations across all operating points. IMEP*, $P_{max}$ and the early combustion phasing (CA10 and CA50) are well reproduced. Importantly, the same set of ECFM-3Z combustion model parameters was used for all the nine operating points, without case-specific retuning; the quality of the agreement therefore supports the robustness of the calibrated model over the entire operating domain investigated.

The AHRR and IMEP* were evaluated as:

$$AHRR = \frac{k}{k-1} p \frac{dV}{d\theta} + \frac{1}{k-1} V \frac{dp}{d\theta} \tag{3}$$

$$IMEP^{*} = \frac{1}{V_d} \int_{IVC}^{EVO} pdV \tag{4}$$

where k is the ratio of specific heats ($k = cp/cv = 1.4$), p and V are the in-cylinder pressure and volume as functions of crank angle θ, and $V_d$ is the engine displacement volume.

A distinctive feature shown by the pressure and AHRR traces in Fig. 6 is the bimodal heat release of the baseline DF cases, which reflects its two-stage Diesel injection. The early pilot auto-ignites first auto-ignites first, producing the smaller peak and initiating the lean $H_2$ flame; the subsequent main injection burns in a diffusion -controlled regime and generates the second, dominant peak, while completing the oxidation of the remaining premixed $H_2$. This two-peak signature is characteristic of late-injection DF operation and is well reproduced across all the calibration points.

A final step of the calibration addressed pollutant emissions, focusing on $CO_2$, CO and $NO_x$. To improve the consistency between simulations and measurements, constant multiplicative correction factors were applied to the raw CFD predictions of each species, following the same procedure previously adopted by the authors in other works. One factor

**Table 5**
Main parameters of the tested operating points of the single cylinder engine.

| IMEP (bar) | 6<br>6<br>6 | | | 12<br>12<br>12 | | | 18<br>18<br>18 | | |
|---|---|---|---|---|---|---|---|---|---|
| $\lambda_g$ (−) | 2.15 | 2.42 | 2.56 | 1.56 | 2.03 | 2.89 | 1.32 | 1.39 | 1.51 |
| $\lambda_{H_2}$ (−) | 3.42 | 3.79 | 4.07 | 2.45 | 3.20 | 4.57 | 4.37 | 4.57 | 4.92 |
| **Boost Pressure (bar)** | 1.27 | 1.36 | 1.46 | 1.91 | 2.30 | 2.87 | 2.69 | 2.80 | 2.89 |
| **Engine speed (rpm)** | 1218 | 1218 | 1218 | 1213 | 1213 | 1213 | 1213 | 1213 | 1213 |
| **Brake Torque (Nm)** | 71.0 | 70.7 | 70.4 | 159.5 | 162.7 | 165.7 | 258.0 | 257.5 | 258.4 |
| **Brake Power (kW)** | 9.0 | 9.0 | 8.9 | 20.2 | 20.6 | 21 | 32.6 | 32.6 | 32.7 |
| **Diesel mass flow rate (kg/h)** | 0.796 | 0.758 | 0.791 | 1.45 | 1.47 | 1.50 | 4.63 | 4.72 | 4.60 |
| **$H_2$ mass flow rate (kg/h)** | 0.6 | 0.6 | 0.6 | 1.14 | 1.14 | 1.15 | 0.91 | 0.91 | 0.91 |
| **Diesel Fuel Mass (mg/cyl/cycle)** | 21.79 | 20.76 | 21.64 | 39.8 | 40.4 | 41.2 | 129.8 | 127.3 | 126.3 |
| **$H_2$ Fuel Mass (mg/cyl/cycle)** | 16.4 | 16.4 | 16.4 | 31.3 | 31.3 | 31.6 | 25.0 | 25.0 | 25.0 |
| **HES (%)** | 67 | 68 | 67 | 69 | 68 | 68 | 35 | 35 | 36 |
| **Swirl ratio @ IVC (−)** | 2.5 | | | | | | | | |
| **Diesel injection strategy** | Pilot + Main | | | | | | | | |
| **Hydrogen injection strategy** | Single Injection | | | | | | | | |
| **EGR (% vol)** | 0 | | | | | | | | |

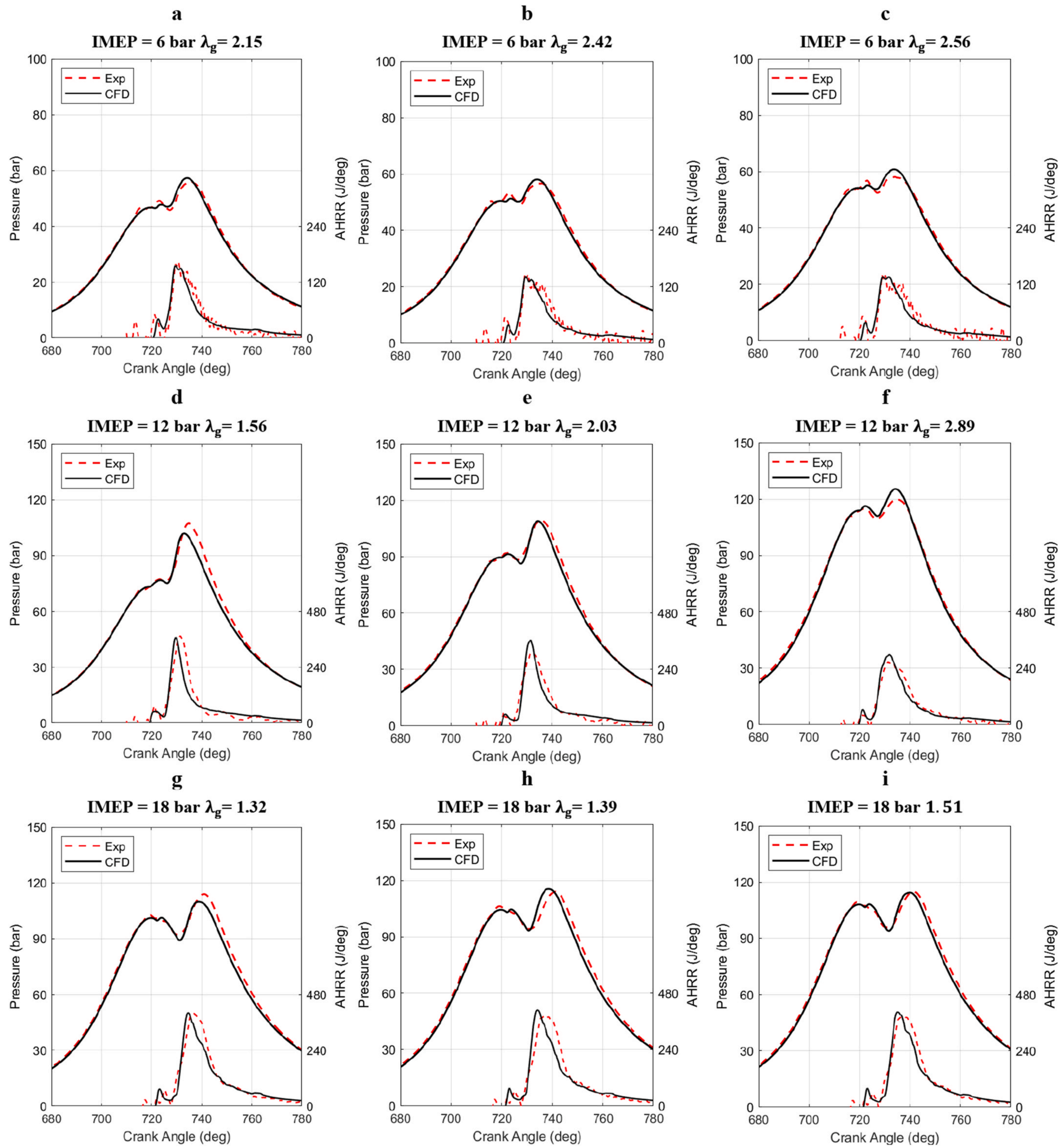


**Fig. 6.** Comparison between experimental and numerical (3D-CFD) in-cylinder pressure and AHRR for the nine calibration points: (a-c) IMEP = 6 bar ($\lambda_g$ = 2.15, 2.42, 2.56); (d-f) IMEP = 12 bar ($\lambda_g$ = 1.56, 2.03, 2.89); (g-i) IMEP = 18 bar ($\lambda_g$ = 1.32, 1.39, 1.51).

was assigned to each pollutant ($CO_2$, CO and $NO_x$) and applied to the simulated values before comparison with the experimental data (Fig. 7a–c). For $CO_2$ and CO, these correction factors can be plausibly related to the use of $C_7H_{16}$ as the Diesel surrogate, whose carbon content and oxidation kinetics may differ from those of the actual fuel used in the tests. An additional contribution to the mismatch in carbon-based emissions likely comes from lubricating-oil combustion, which cannot be represented in the present 3D-CFD framework, as oil consumption is not modelled. After applying the correction factors, the agreement between simulated and measured emissions is, on average, satisfactory over the full set of operating points, and the model correctly reproduces the dominant trends: $CO_2$ and CO increase with engine load as the injected Diesel mass rises (see Table 5), while $NO_x$ increases mainly as a consequence of the higher in-cylinder temperatures and pressures at higher load.

During the experimental campaign, the external EGR system was

**Table 6**
Initial conditions at IVC and wall temperatures imposed in the 3D-CFD simulations for the nine calibration points.

| IMEP (bar) | 6<br>6<br>6 | | | 12<br>12<br>12 | | | 18<br>18<br>18 | | |
|---|---|---|---|---|---|---|---|---|---|
| $\lambda_g$ (−) | 2.15 | 2.42 | 2.56 | 1.56 | 2.03 | 2.89 | 1.32 | 1.39 | 1.51 |
| **$T_{IVC}$ (K)** | 397 | 387 | 390 | 442 | 418 | 366 | 451 | 446 | 425 |
| **$P_{IVC}$ (bar)** | 1.59 | 1.70 | 1.82 | 2.53 | 3.01 | 3.67 | 3.44 | 3.53 | 3.61 |
| **$m_{IVC}$ (mg)** | 1925 | 2133 | 2289 | 2642 | 3438 | 4950 | 3746 | 3908 | 4217 |
| **$T_{Piston}$ (K)** | 550 | | | | | | | | |
| **$T_{Liner}$ (K)** | 480 | | | | | | | | |
| **$T_{Head}$ (K)** | 500 | | | | | | | | |
| **$T_{int\_val}$ (K)** | 450 | | | | | | | | |
| **$T_{exh\_val}$ (K)** | 550 | | | | | | | | |

**Table 7**
Comparison between experimental and numerical (3D-CFD) IMEP*; $P_{max}$; PPRR; combustion phasing parameters for the low-load operating point (IMEP = 6 bar).

| Engine Parameter | IMEP = 6 bar | | | | | | | | |
|---|---|---|---|---|---|---|---|---|---|
| | $\lambda_g = 2.15$ | | $\lambda_g = 2.42$ | | $\lambda_g = 2.56$ | | Absolute error | | |
| | Exp. | Sim | Exp. | Sim | Exp. | Sim | $\lambda_g = 2.15$ | $\lambda_g = 2.42$ | $\lambda_g = 2.56$ |
| **IMEP* (bar)** | 6.40 | 6.70 | 6.42 | 6.64 | 6.45 | 6.72 | 0.30 | 0.22 | 0.28 |
| **Peak in-cylinder Pressure (bar)** | 56.6 | 57.3 | 57.24 | 58.0 | 58.8 | 60.9 | 0.70 | 0.86 | 2.10 |
| **PPRR (bar/deg)** | 2.56 | 2.61 | 2.63 | 2.069 | 2.31 | 1.87 | 0.05 | 0.19 | 0.45 |
| **CA10 (° CA aFTDC)** | 728.2 | 728.9 | 728.3 | 728.8 | 728.2 | 728.8 | 0.7 | 0.5 | 0.6 |
| **CA50 (° CA aFTDC)** | 735.1 | 735.4 | 736.1 | 736.1 | 736.7 | 736.2 | 0.3 | 0.0 | 0.5 |
| **CA90 (° CA aFTDC)** | 757.0 | 770.8 | 761.7 | 771.7 | 762.0 | 771.8 | 13.8 | 10.0 | 9.8 |

**Table 8**
Comparison between experimental and numerical (3D-CFD) IMEP*; $P_{max}$; PPRR; combustion phasing parameters for the mid-load operating point (IMEP = 12 bar).

| Engine Parameter | IMEP = 12 bar | | | | | | | | |
|---|---|---|---|---|---|---|---|---|---|
| | $\lambda_g = 1.56$ | | $\lambda_g = 2.03$ | | $\lambda_g = 2.89$ | | Absolute error | | |
| | Exp. | Sim | Exp. | Sim | Exp. | Sim | $\lambda_g = 1.56$ | $\lambda_g = 2.03$ | $\lambda_g = 2.89$ |
| **IMEP* (bar)** | 12.38 | 12.08 | 12.52 | 12.71 | 12.68 | 13.41 | 0.30 | 0.19 | 0.70 |
| **Peak in-cylinder Pressure (bar)** | 107.5 | 101.8 | 109.9 | 109.0 | 125.4 | 119.9 | 5.7 | 0.0 | 5.1 |
| **PPRR (bar/deg)** | 5.88 | 7.23 | 3.90 | 6.23 | 3.54 | 3.65 | 1.35 | 2.33 | 0.11 |
| **CA10 (° CA aFTDC)** | 727.6 | 727.7 | 728.6 | 729.2 | 728.8 | 728.4 | 0.1 | 0.6 | 0.4 |
| **CA50 (° CA aFTDC)** | 733.1 | 734.2 | 734.8 | 735.5 | 735.9 | 735.4 | 1.2 | 0.7 | 0.5 |
| **CA90 (° CA aFTDC)** | 755.6 | 773.7 | 753.4 | 771.6 | 753.0 | 767.5 | 18.1 | 18.2 | 14.5 |

**Table 9**
Comparison between experimental and numerical (3D-CFD) IMEP*; $P_{max}$; PPRR; combustion phasing parameters for the high-load operating point (IMEP = 18 bar).

| Engine Parameter | IMEP = 18 bar | | | | | | | | |
|---|---|---|---|---|---|---|---|---|---|
| | $\lambda_g = 1.32$ | | $\lambda_g = 1.39$ | | $\lambda_g = 1.51$ | | Absolute error | | |
| | Exp. | Sim | Exp. | Sim | Exp. | Sim | $\lambda_g = 1.32$ | $\lambda_g = 1.39$ | $\lambda_g = 1.51$ |
| **IMEP* (bar)** | 18.46 | 18.00 | 18.49 | 18.20 | 18.62 | 18.41 | 0.46 | 0.29 | 0.21 |
| **Peak in-cylinder Pressure (bar)** | 114.1 | 109.8 | 114.0 | 115.4 | 115.0 | 114.5 | 4.3 | 1.4 | 0.5 |
| **PPRR (bar/deg)** | 5.44 | 5.00 | 5.35 | 5.15 | 5.39 | 4.63 | 0.44 | 0.20 | 0.76 |
| **CA10 (° CA aFTDC)** | 732.5 | 732.7 | 732.8 | 732.2 | 733.0 | 732.9 | 0.2 | 0.6 | 0.1 |
| **CA50 (° CA aFTDC)** | 740.2 | 741.1 | 740.6 | 740.2 | 740.8 | 740.7 | 0.9 | 0.4 | 0.1 |
| **CA90 (° CA aFTDC)** | 766.4 | 779.6 | 766.1 | 776.8 | 766.2 | 774.7 | 13.2 | 10.7 | 8.5 |

switched off and the 2IVO event in the intake valve lift profile was kept very narrow (see Fig. 2), resulting in a negligible amount of internal EGR. Accordingly, the EGR mass fraction was set to zero in all simulations.

Overall, these results indicate that the calibrated 3D-CFD model is able to capture the main mechanisms and trends of pollutant formation in DF operation, and can therefore be reliably used for relative emission assessments in the subsequent optimization study, even though absolute emission levels should be interpreted with caution.

### *2.4. Injection optimization*

The optimization was carried out on the calibrated DF operating point, characterized by an IMEP of 6 bar, $\lambda_g = 2.56$ and $\lambda_{H2} = 4.07$ (see Table 5). Among the three low-load conditions, this operating point corresponds to the highest boost level and is therefore the one with the highest global excess-air ratio and the highest $H_2$ excess-air ratio. This combination of strong global dilution and $H_2$-lean operation makes the selected case particularly suitable as a baseline for the optimization: starting from the most diluted condition provides additional margin to increase the HES while keeping $NO_x$ formation under control. In

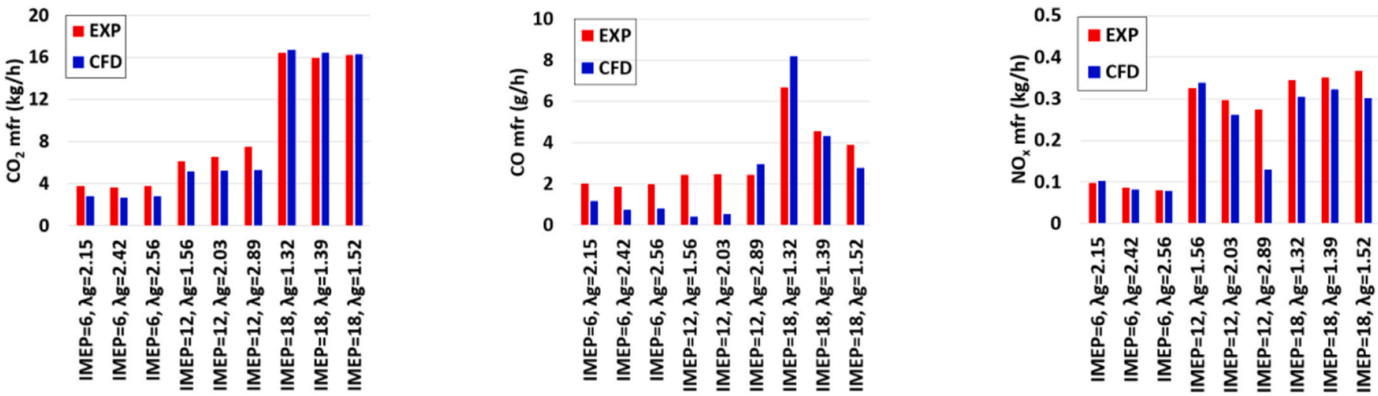


**Fig. 7.** Comparison between experimental and numerical (3D-CFD) emissions: a) $CO_2$, b) CO and c) $NO_x$.

addition, operating at partial load offers a wider safety margin with respect to the mechanical limits of the engine in the presence of $H_2$ combustion, since the intrinsically faster burning rate and steeper heat-release profiles associated with $H_2$ can be more safely controlled at low load, helping to maintain $P_{max}$ and PPRR within acceptable bounds. For these reasons, this operating point was selected as the baseline condition for the injection-optimization study.

The optimization campaign was conducted by progressively modifying the Diesel injection strategy and the Diesel–$H_2$ energy split. The underlying idea was to reduce as much as possible the amount of Diesel required to sustain stable combustion, while compensating the removed Diesel energy with additional $H_2$ so as to preserve the overall energy provided to the engine. Starting from the baseline DF case, the main Diesel injection was completely removed and only the pilot event was retained. Three ultra-high HES fuelling configurations were then defined by acting on the mass of the single Diesel pilot injection and on the $H_2$ flow rate. The first configuration, with HES = 96%, corresponds to the case in which the Diesel pilot injection maintains the same mass as in the baseline dual-injection strategy, while the energy contribution of the main is entirely replaced by additional $H_2$. Two further configurations were generated by progressively reducing the pilot Diesel mass, leading to operating points with HES = 98% and HES = 99%, respectively. In all Diesel-reduced conditions, the total fuel energy input was kept equal to the baseline, but the relative contribution of Diesel and $H_2$ was strongly shifted in favour of $H_2$.

The baseline DF injection law (HES = 67%) and the three Diesel-reduced single-pilot strategies at HES = 96%, 98% and 99% are compared in Fig. 8, which reports the Diesel injection-velocity profiles as a function of crank angle. The baseline case exhibits the original pilot-main split strategy, whereas the Diesel-reduced cases are characterised by the disappearance of the main injection and by a progressive shortening of the pilot duration as HES increases. In Fig. 8, the curves represent the injection velocity imposed at the nozzle outlet and used to initialise the Diesel parcels in the fluid domain. A key modelling assumption is that the injection system can deliver the reduced pilot quantities with approximately the same peak injection velocity as in the baseline, while the lower injected mass is achieved by shortening the injection duration. Consequently, the single-pilot strategies appear as increasingly narrow as the HES rises from 96% to 99%. This assumption is considered realistic from an experimental standpoint, in view of the high level of controllability of the common-rail Diesel systems and the relatively low engine speed of the present study (about 1200 rpm).

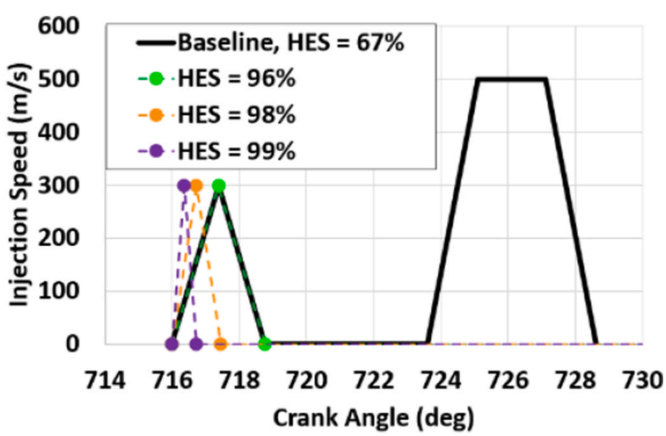


**Fig. 8.** Comparison between Diesel injection-velocity profiles for the baseline DF pilot–main strategy (IMEP = 6 bar, HES = 67%) and the optimized single-pilot injection laws at HES = 96%, 98% and 99%.

The purpose of the subsequent DOE was to assess how the timing of these small pilot injections influences the combustion process at ultra-high HES, in particular when the Diesel is injected early enough to achieve a more extensively premixed in-cylinder distribution. By considering pilot SOI values ranging from moderately to strongly advanced, the study was designed to span a continuum of conditions in which the Diesel ranges from relatively stratified to significantly more homogeneous.

To this end, a DOE on the pilot SOI was carried out for each of the three fuelling configurations: HES = 96%, 98% and 99%. In all simulations, the operating condition described above was retained, together with the same boundary conditions, wall temperatures and numerical settings used in the calibration phase. In addition, the mass of air trapped in the cylinder was kept approximately constant across the different HES levels and SOI settings. In a real engine, port fuel injection of $H_2$ would tend to reduce the $\lambda_v$ [53,54], since the low-density gaseous fuel occupies part of the intake volume and displaces air, thereby decreasing the trapped air mass. In the present work, however, this effect was deliberately neglected and compensated. Thanks to the electro-actuated and fully independent boosting system available on the engine test bench, the intake pressure can be adjusted to counteract the $\lambda_v$ penalty associated with $H_2$ port fuel injection. Since the focus of the study is on the influence of HES and Diesel injection timing on combustion and emissions, rather than on the secondary effects of $H_2$ injection such as $\lambda_v$ loss, the trapped air mass was therefore held approximately constant to isolate as much as possible the role of HES in the observed combustion behaviour. The Diesel injection velocity was kept constant. As a result, within each HES level, the only control parameter varied in the DOE was the SOI of the single Diesel pilot event. A related assumption concerns the port fuel injection of $H_2$. Although the progressive Diesel-to-$H_2$ substitution increases the $H_2$ concentration in the intake, the charge remains ultra-lean over the entire HES range explored, as confirmed later by the $\lambda_{H2}$ values which stay well above stoichiometric. This ultra-lean character, combined with the low-load operating condition, the Miller-cycle LIVC that lowers the effective compression ratio and charge temperature, and the deactivated EGR, minimizes the hot residual gases and in-cylinder hot spots that trigger backfire. The onset of backfire or pre-ignition is therefore unlikely and was neglected, allowing the closed-valve (IVC-to-EVO) simulation methodology to remain accurate.

The SOI was swept over a wide range of crank angles, specifically, the SOI was varied from 645°CA to 710°CA with a 5°CA increment, and from 710°CA to 720°CA with a finer 2°CA step. For each HES level, this resulted in a matrix of pilot timings.

For every HES–SOI combination included in the DOE, a consistent set of performance indicators was extracted from the 3D-CFD results to assess the suitability of the corresponding injection law. The analysis considered the GIE, the achieved IMEP*, $P_{max}$ and PPRR, as well as the combustion phasing and duration, quantified through CA10, CA50, CA90 and the CA10–90 interval. The combustion efficiency ($\eta_c$) is also evaluated to ensure that the reduction in Diesel quantity does not lead to excessively incomplete combustion.

On the emissions side, the main parameters of interest were the $CO_2$, CO and $NO_x$ mass flow rates, together with the amount of unburned $H_2$ at exhaust.

## 3. Results

### 3.1. Effect of HES and pilot timing on ηc and emissions

The DOE was performed to assess the effects of the SOI of the single Diesel pilot on combustion and emissions under ultra-high HES conditions. The starting point of the analysis was the baseline low-load operating case (IMEP = 6 bar), characterised by $\lambda_g \approx 2.56$. All additional cases were derived from this reference condition, maintaining the same trapped air mass, total fuel energy input, boundary conditions, wall temperatures and numerical settings.

The main performance parameters of the three fuelling configurations (HES = 96%, 98% and 99%) are summarized in Table 10, together with the baseline DF case (HES = 67%). As anticipated in the previous chapter, the shift from the baseline DF case to the Diesel-reduced configurations was achieved by progressively decreasing the Diesel mass flow rate and compensating the removed energy with additional $H_2$, while keeping the total fuel energy input constant. Moving from 67% to 96–99% HES results in a very large reduction of the injected Diesel quantity (−88.4% at HES = 96%, up to −97.0% at HES = 99%) and a corresponding increase in $H_2$ mass flow rate (+44 to +47%).

Since the trapped air mass was held approximately constant, the variations in the $\lambda_g$ and $\lambda_{H2}$ directly reflect the change in fuel split. This behaviour can be interpreted in terms of the relative Low Heating Value (LHV*; see Equation (5)), defined as the ratio between the fuel Lower Heating Value (LHV) and the stoichiometric air-fuel mass ratio ($\alpha_{st}$), and therefore expressing the amount of heat released by a stoichiometric air-fuel mixture per unit mass of air. In the present work the Diesel fuel is represented by its n-heptane surrogate, for which LHV = 44.4 MJ/kg and $\alpha_{st} = 15.2$ [52], while for $H_2$ LHV = 120 MJ/kg and $\alpha_{st} = 34.1$ [55, 56]. The resulting LHV* therefore $LHV^*_{H_2} \approx 3.52$ MJ/kg for $H_2$ and $LHV^*_D \approx 2.98$ MJ/kg for $C_7H_{16}$. $H_2$ is characterized by a significantly higher LHV* than $C_7H_{16}$; as consequence, for a given trapped air mass and constant total fuel energy input, progressively replacing Diesel with $H_2$ requires a smaller total fuel mass and leads to a gradual leaning of the overall mixture. This effect is reflected in Table 10 by a moderate increase in $\lambda_g$ (from 2.56 to about 2.73) and a simultaneous decrease in $\lambda_{H2}$ (from 4.07 to about 2.76). At the highest HES values, the contribution of Diesel to the $\lambda_g$ becomes marginal, so that $\lambda_g$ naturally tends towards $\lambda_{H_2}$. This convergence is fully consistent with the fact that, in ultra-high HES conditions, the mixture behaviour is essentially governed by $H_2$. In all the cases, $\lambda_{H2}$ remains well above stoichiometric values, confirming that the $H_2$-air mixture is ultra-lean, a key prerequisite for limiting flame temperatures and, consequently, thermal $NO_x$ formation.

$$LHV^* = \frac{LHV}{\alpha_{st}} \tag{5}$$

Fig. 9a–c reports the in-cylinder pressure and AHRR traces obtained from the DOE for the three ultra-high HES single-pilot configurations. For the sake of clarity, only cases with pilot SOI up to 710°CA are shown, although the DOE covered a wider range up to 720°CA. For all HES levels, simulations with SOI later than 710°CA exhibited severely deteriorated combustion, with almost overlapping pressure expansion curves and negligible heat release; these cases were therefore omitted from Fig. 9, as they do not provide additional insight.

Among the studied HES, the most critical behaviour was observed at HES = 99% (Fig. 9 c). For the most advanced timings (SOI = 645°, 650° and 655°CA), no appreciable combustion develops and the pressure traces remain close to motored conditions. For SOI between 660° and 710°CA, combustion does occur but the expansion pressure remains significantly lower than in the baseline DF case and the corresponding AHRR peaks are very modest, indicating poor combustion efficiency. This behaviour confirms that, at 99% HES, the energy released by the strongly reduced Diesel quantity is insufficient to reliably initiate the premixed combustion of the ultra-lean $H_2$–air mixture, regardless of the injection timing.

For HES = 96% and HES = 98% (Fig. 9a–b), a similar trend is observed for the most advanced timings. In both cases, SOI = 645°CA is too early to induce a stable combustion. At HES = 96%, combustion becomes stable starting from SOI = 650°CA. In this configuration, the Diesel pilot is injected approximately 70°CA before TDC, allowing extensive premixing before auto-ignition occurs. Under these highly premixed conditions, Diesel auto-ignites with combustion phasing comparable to that of the baseline Dual Fuel case. However, unlike the baseline configuration, characterised by two Diesel injection events (pilot and main) and a corresponding two-peak heat release profile typical for this late-injection DF operation, the AHRR now exhibits a single peak. This shape of the AHRR reflects the transition from a conventional pilot-ignited DF regime to a RCCI regime.

As the pilot SOI is progressively retarded from 650°CA toward 680°CA, the start of combustion advances in terms of crank angle. This counterintuitive behaviour arises because the pilot is injected under increasingly favourable thermodynamic conditions (higher temperature), resulting in a shorter ignition delay and a more abrupt auto-ignition event. The AHRR traces for SOI = 655°, 660° and 680°CA display pronounced and sharper peaks, indicating a more energetic ignition of the $H_2$–air mixture. This is accompanied by a clear increase in $P_{max}$.

Delaying the pilot injection to SOI = 690° and 700°CA leads to an even earlier auto-ignition. However, when the injection timing

**Table 10**
Comparison between the baseline DF operating point (IMEP = 6 bar, λg = 2.56) and the ultra-high HES single-pilot configurations in terms of excess-air ratios and fuel mass flow rates.

| HES | $\lambda_g$ | | $\lambda_{H_2}$ | | Injected Diesel (g/h) | | Injected hydrogen (g/h) | |
|---|---|---|---|---|---|---|---|---|
| | val. | Δ% | val. | Δ% | val. | Δ% | val. | Δ% |
| 67% (baseline) | 2.56 | 0 | 4.07 | 0 | 791 | 0 | 600 | 0 |
| 96% | 2.71 | +5.86 | 2.84 | −30.2 | 92 | −88.4 | 860 | +44.1 |
| 98% | 2.72 | +6.25 | 2.78 | −31.5 | 48 | −93.9 | 870 | +46.1 |
| 99% | 2.73 | +6.64 | 2.76 | −32.2 | 24 | −97.0 | 880 | +47.3 |

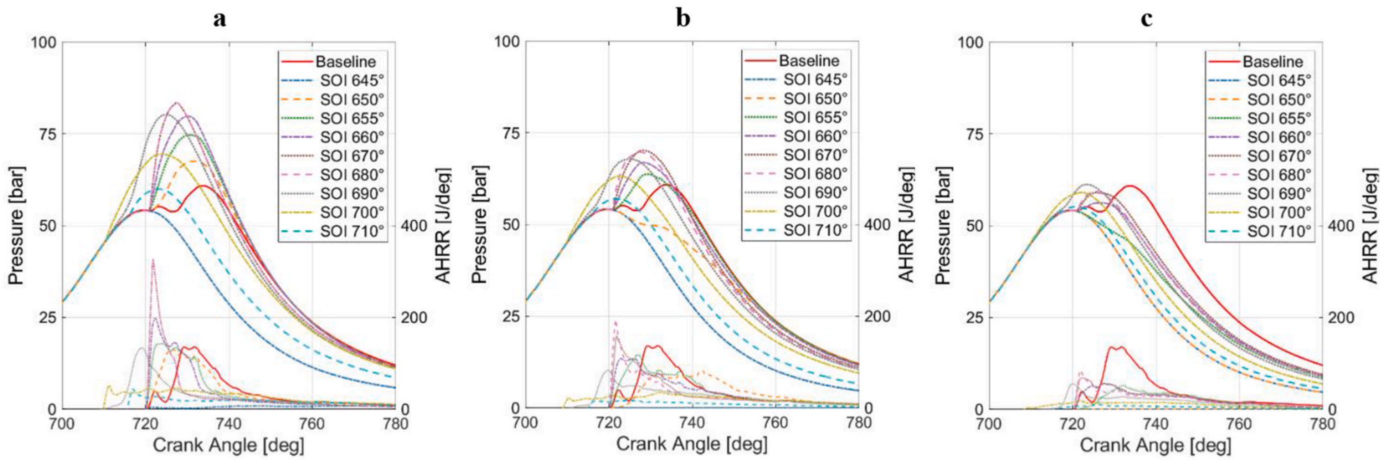


**Fig. 9.** In-cylinder pressure and AHRR traces for the ultra-high HES single-pilot configurations (HES = 96% (a), 98% (b) and 99% (c)) obtained from the DOE, compared with the baseline DF case. Results are shown for pilot SOI values up to 710°CA.

approaches SOI ≈710°CA, the pilot is introduced too late in the compression stroke to effectively trigger stable $H_2$ combustion.

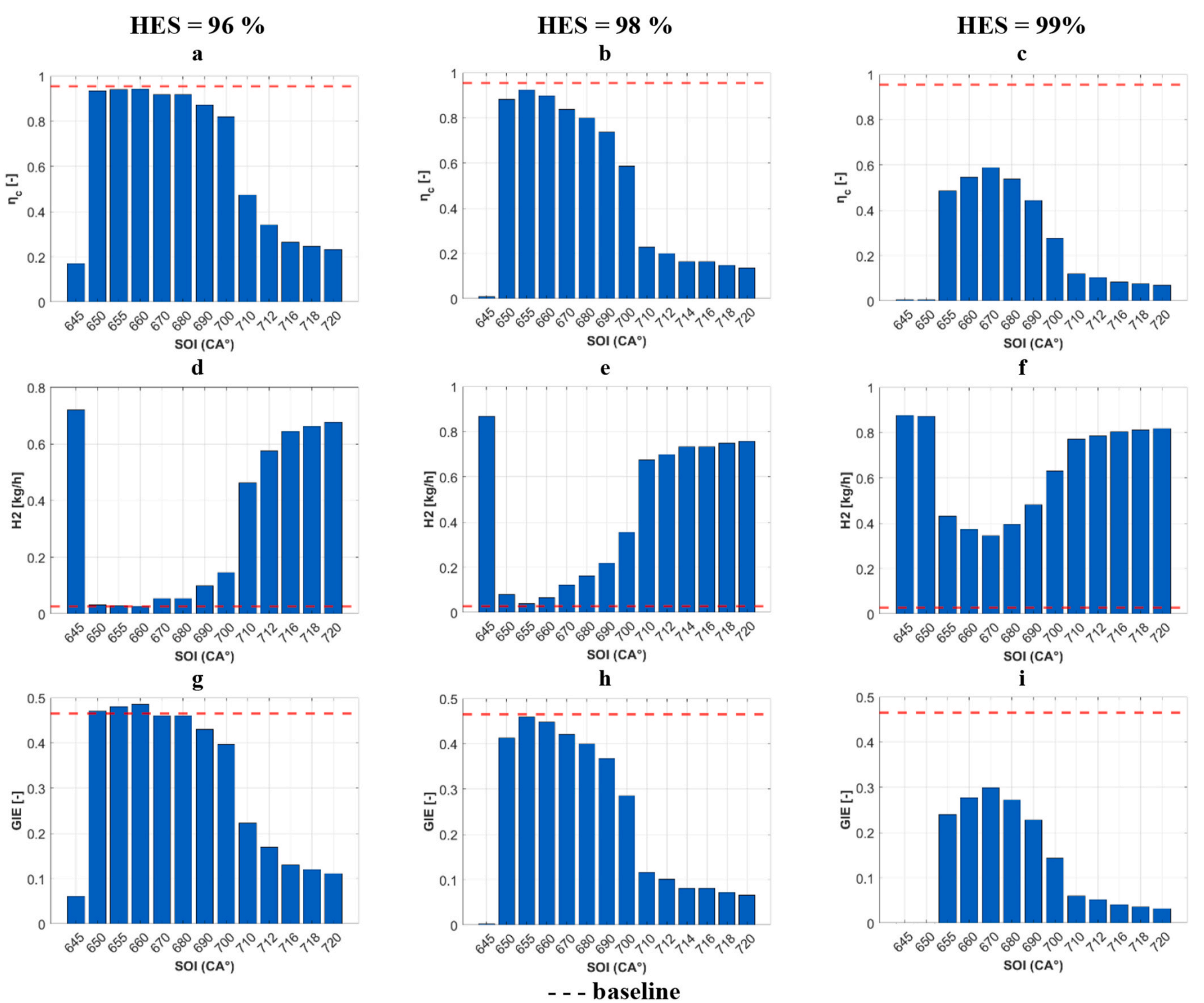


**Fig. 10.** $\eta_c$, $H_2$ mass flow rate at exhaust and GIE for all DOE cases at different HES, compared with the baseline DF configuration. a-c) show $\eta_c$ d-f) show $H_2$ mass flow rate at exhaust and g-i) show GIE as a function of pilot SOI for HES = 96%, 98% and 99%, respectively.

The HES = 98% cases exhibit trends that are qualitatively very similar to those observed at HES = 96%, with a comparable evolution of pressure and AHRR as the pilot SOI is varied. This configuration can therefore be regarded as the upper practical limit in terms of HES: as previously discussed for HES = 99%, the strongly reduced Diesel quantity is no longer able to sustain $H_2$ combustion in a robust way for any of the tested SOI values.

Fig. 10 summarize the influence of pilot SOI on combustion completeness and global efficiency for the three ultra-high HES single-pilot configurations, in comparison with the baseline DF case. Fig. 10a–c report $\eta_c$ as a function of SOI for HES = 96%, 98% and 99%, respectively; Fig. 10d–f show the corresponding $H_2$ mass flow rate at exhaust valve opening; Fig. 10g–i present the GIE. In all plots, the baseline configuration is indicated by a red dashed line.

For HES = 96% (Fig. 10 a) and 650°CA < SOI <680°CA, $\eta_c$ remains relatively close to the baseline but systematically lower. As the pilot is retarded from 680° to 710°CA, a decrease in $\eta_c$ is observed. The HES = 98% configuration (Fig. 10 b) follows a similar trend, with overall lower $\eta_c$ values and a narrower SOI interval ensuring acceptable combustion completeness, consistently with the further reduction in Diesel quantity.

Two distinct mechanisms govern the residual unburned $H_2$, and their relative weight changes with HES and pilot SOI. The first is the near-wall and crevice quenching of the lean $H_2$ flame, intrinsic to ultra-lean premixed $H_2$ combustion and present also in the baseline, where the residual $H_2$ is located in the peripheral squish and crevice regions. The second, which becomes dominant in the single-pilot RCCI configurations, is a local reactivity deficit in the central region of the bowl: the spray cone and the re-entrant bowl, both designed for conventional pilot-ignited Diesel combustion, leave the bowl core essentially unreached by the high-reactivity fuel, so that the lean $H_2$–air charge there lacks a local ignition source and forms a central unburned pocket, whose spatial structure is examined through the in-cylinder maps presented below. Within the stable SOI window at HES = 96%, the more homogeneous and faster premixed combustion actually improves peripheral conversion, so that the overall unburned-$H_2$ fraction at EVO is lower than in the baseline (3.02% vs 4.55%); the modest ηc reduction is therefore driven mainly by incomplete Diesel oxidation rather than by increased $H_2$ slip. As the pilot mass is further reduced at HES = 98%, the central reactivity deficit intensifies, the central pocket grows and the unburned $H_2$ rises to 4.38%.

At the extremes of the SOI sweep, by contrast, the marked increase in unburned $H_2$ shown in Fig. 10d–f stems from neither of these two mechanisms. Here the Diesel pilot is unable to ignite the ultra-lean $H_2$–air charge in the first place (being injected either too early to establish a stable auto-ignition or too late in the compression stroke to trigger it) so that combustion becomes globally incomplete rather than leaving the localized central pocket observed within the stable SOI window.

Despite the reduction in combustion efficiency, some operating points at HES = 96% exhibit a higher GIE than the baseline (Fig. 10 g). The best case reach GIE ≈0.485, compared with 0.465 of the baseline with a SOI = 655°CA. This improvement is linked to the faster heat release rate at higher $H_2$ content, which yield a more favourable combustion phasing and a higher thermodynamic efficiency of the cycle. At HES = 98%, the GIE follows the same qualitative behaviour but with slightly lower peak values, reflecting the more delicate balance between reduced Diesel quantity, combustion completeness and thermodynamic benefits.

The HES = 99% configuration (Fig. 10c–f,i) is reported only for the sake of completeness. In this case, combustion efficiency remains low for all SOI values (typically below 60%), the $H_2$ mass flow rate at exhaust is high over the whole SOI sweep of injection timing, and the GIE never approaches the baseline level: even in the most favourable case (around SOI = 670°CA), GIE is approximately half of the baseline value. These results confirm that, at 99% HES, the strongly reduced Diesel quantity is unable to sustain $H_2$ combustion in a robust manner.

Overall, Fig. 10 shows that HES = 96% and 98% can sustain stable combustion over a limited SOI range, but at the cost of a systematic decrease in combustion efficiency and higher unburned $H_2$ at exhaust. At the same time, selected operating points at HES = 96% can achieve a higher GIE than the baseline. This highlights a clear trade-off between combustion completeness and thermodynamic efficiency that must be carefully considered in the selection of the optimal combination of HES and injection timing in the subsequent performance and emissions analysis. Fig. 11(a–i) summarizes the evolution of emissions over the entire DOE matrix for the three ultra-high HES configurations, compared with the baseline DF case. Fig. 11(a–c) report $CO_2$ emissions, Fig. 11 (d–f) show CO, and Fig. 11(g–i) present $NO_x$ for HES = 96%, 98% and 99%, respectively. In all plots, the baseline configuration is indicated by a red dashed line.

Since the emission levels of the different configurations span more than one order of magnitude, the concentrations expressed in ppm are reported using a logarithmic scale, in order to preserve both the visibility of the ultra-low emission cases and the resolution at higher values coming from incomplete combustions.

As expected, $CO_2$ emissions decrease with increasing HES, reflecting the progressive reduction of Diesel consumption. For each SOI sweep, moving from the baseline case (HES = 67%) to HES = 96%, 98% and 99% leads to a marked drop in $CO_2$ mass flow rate.

The behaviour of CO emissions is more complex and only partly tracks combustion efficiency. At HES = 96%, the cases with the highest $\eta_c$ exhibit low CO levels, lower than the baseline, because the small amount of Diesel that reacts oxidises efficiently through to $CO_2$. For lower combustion efficiencies, particularly at very retarded timings (SOI >710°CA), the oxidation process deteriorates more broadly: a larger fraction of $H_2$ remains unburned and the Diesel is only partially oxidised, so that CO rises sharply and exceed the baseline level.

At HES = 98%, the same qualitative trend is observed, but shifted towards higher CO levels. The generally lower combustion efficiencies, associated with the reduced Diesel quantity, make Diesel oxidation less complete over a wider portion of the timing range, so that CO emissions tend to increase for a larger number of SOI values. In the HES = 99% configuration, CO levels are consistently higher than in the baseline case for all tested SOI values, in line with the very poor combustion quality already highlighted by $\eta_c$ and $H_2$ residuals.

The $NO_x$ emissions reported in Fig. 11g–i exhibit a clear and consistent behaviour. All ultra-high HES cases produce lower $NO_x$ than the baseline DF configuration, and, for a given SOI, $NO_x$ systematically decreases as HES increases. This trend reflects the gradual transition from a Diesel combustion mode towards a premixed and more homogeneous $H_2$ combustion, with $\lambda_{H2}$ remaining very high ($\lambda_{H2} > 2.50$) and the contribution of diffusion-controlled Diesel burning progressively reduced. As the Diesel mass decreases, the typical Diesel hot spots disappear, and the conditions favourable to thermal $NO_x$ formation are strongly limited.

Within each HES level, $NO_x$ emissions also show a marked dependence on pilot SOI. Very advanced injections, corresponding to strongly or partially premixed Diesel combustion, yield the lowest $NO_x$ emissions levels. In these cases, the early-injected pilot has sufficient time to mix with the charge, acting as a distributed ignition source for $H_2$ and promoting a more uniform temperature field, rather than the more localised auto-ignition regions observed for retarded SOI. As the SOI is shifted towards and beyond 700°CA, the behaviour progressively approaches that of a conventional DF Diesel operation: the Diesel is injected later, has less time to mix, and burns under more stratified conditions, generating local high-temperature regions and, consequently, higher $NO_x$.

Overall, Fig. 11g–i indicates that $NO_x$ emissions are governed by the combined effect of HES and SOI. Increasing HES moves the system from a Diesel combustion mode to an ultra-lean, premixed $H_2$ combustion operation, reducing the intrinsic tendency to form $NO_x$. For a given HES,

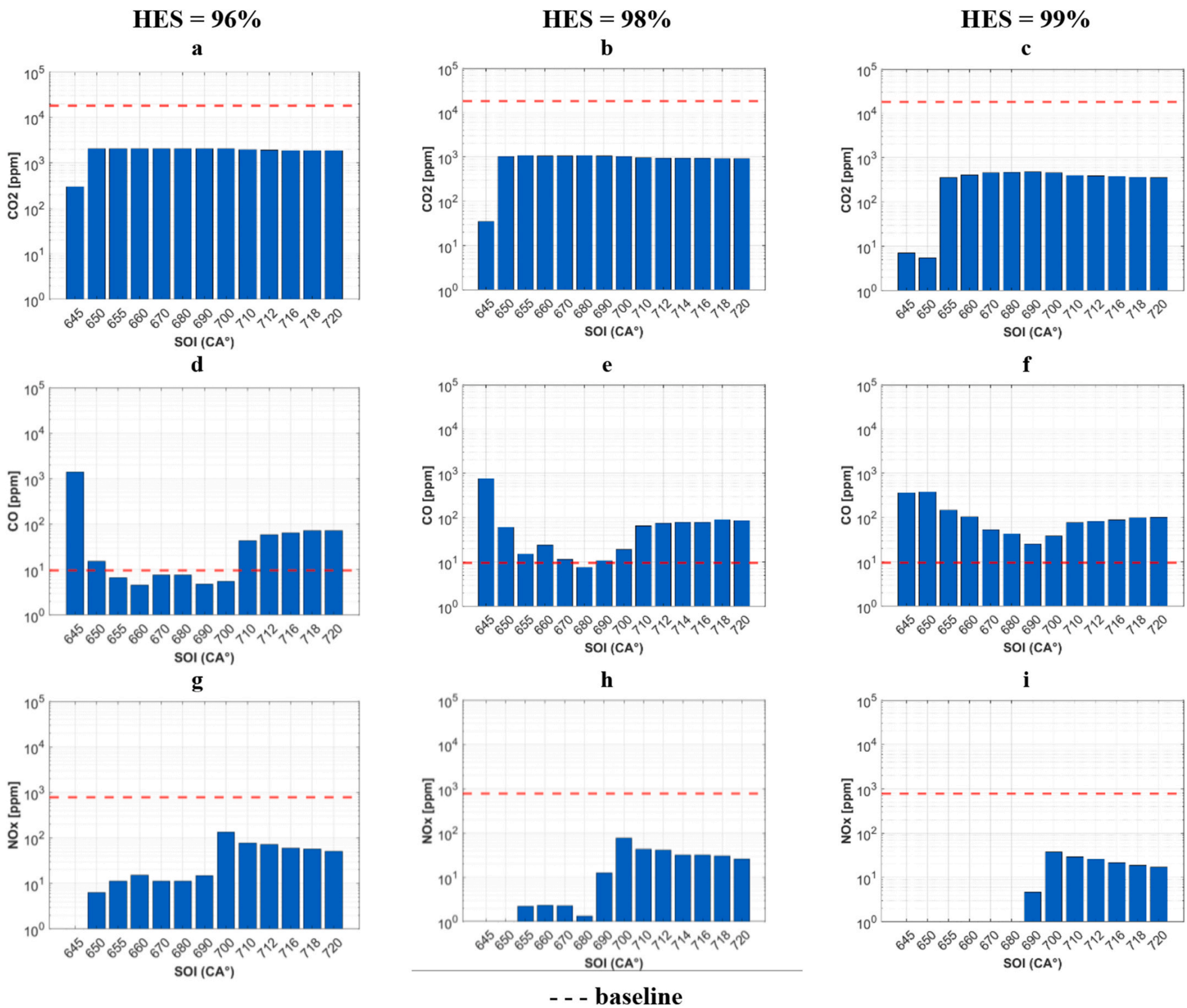


**Fig. 11.** $CO_2$, CO and $NO_x$ emissions for all DOE cases at different HES, compared with the baseline DF configuration. a–c) show $CO_2$; d–f) show CO and g-i) show $NO_x$ as a function of pilot SOI for HES = 96%, 98% and 99%, respectively.

advancing the pilot SOI enhances premixing and temperature uniformity, further suppressing $NO_x$ emissions, whereas late injections reintroduce stratification and temperature hot spots. In this framework, the most advanced, ultra-lean cases can be regarded as approaching an RCCI combustion regime, a concept that will be further explored in the following analysis of the in-cylinder temperature and heat release characteristics.

### *3.2. Selection and characterization of optimized ultra-high HES operating points*

On the basis of the DOE results discussed in the previous section, two ultra-high HES operating points were selected as the optimal configurations. The main goal was to limit the performance penalty associated with the ultra-high HES conversion while achieving a substantial reduction of emissions within the engine mechanical limits. Accordingly, the retained configurations were those combining.

- the highest attainable IMEP*, as close as possible to, or above, the baseline load;
- the highest attainable GIE, matching or exceeding that of the baseline;
- a substantial reduction of $CO_2$ and $NO_x$ emissions with respect to the baseline;
- $P_{max}$ and PRR within the structural limits of the engine.

Among all the simulated cases, the following configurations emerged as the most favourable compromise between performance and emissions.

- HES = 96%, SOI = 660°CA, which minimizes $NO_x$ emissions while providing a 4.4% increase in GIE compared with the baseline;
- HES = 98%, SOI = 655°CA, which achieves near-zero $NO_x$ emissions with the lowest GIE penalty among all tested 98% HES cases.

The main performance and emission metrics for these two operating points, compared with the baseline DF configuration, are summarized in Tables 11 and 12. The tables report GIE, $P_{max}$, combustion duration (CA10–90), $\eta_c$, and $CO_2$, CO and $NO_x$ emissions, together with their relative deviations with respect to the baseline.

**Table 11**
Comparison between baseline and optimized RCCI cases (HES = 96%, 98%), in terms of GIE, $P_{max}$, PPRR, Combustion duration and ηc.

| | GIE | | $P_{max}$ | | PPRR | | CA10-90 | | $\eta_c$ | |
|---|---|---|---|---|---|---|---|---|---|---|
| | val. | Δ% | val. | Δ% | val. | Δ% | val. | Δ% | val. | Δ% |
| | (bar) | (%) | (bar) | (%) | (bar/deg) | (%) | (° CA) | (%) | (–) | (%) |
| Baseline HES = 67% | 0.465 | 0 | 60.9 | 0 | 1.87 | 0 | 43.6 | 0 | 0.96 | 0 |
| HES = 96% | 0.485 | +4.4 | 79.8 | +31 | 6.28 | +237 | 31.5 | −12.1 | 0.94 | −1.3 |
| HES = 98% | 0.459 | −1.2 | 63.7 | +5 | 2.57 | +37 | 33.4 | −10.2 | 0.93 | −3.2 |

**Table 12**
Comparison between baseline and optimized RCCI cases (HES = 96%, 98%), in terms of $CO_2$, CO, $NO_x$ emissions, unburned $H_2$ and hydrocarbons (HC).

| | $CO_2$ | | CO | | $NO_x$ | | Unburned $H_2$ | | Unburned HC | |
|---|---|---|---|---|---|---|---|---|---|---|
| | val. | Δ%. | val. | Δ% | val. | Δ% | val. | Δ% | val. | Δ% |
| | (kg/h) | (%) | (g/h) | (%) | (ppm) | (%) | (g/h) | (%) | (mg/h) | (%) |
| Baseline HES = 67% | 2.81 | 0 | 0.81 | 0 | 855 | 0 | 27.2 | 0 | 33.8 | 0 |
| HES = 96% | 0.32 | −88.6 | 0.39 | −52 | 16.83 | −98.0 | 26.0 | −4.4 | 44.9 | +32.7 |
| HES = 98% | 0.17 | −94.0 | 1.30 | +60 | 2.44 | −99.7 | 38.3 | +40.8 | 7.08 | −79.1 |

Tables 11 and 12 highlight several key features of the optimized configurations. Both ultra-high HES cases exhibit a shorter combustion duration (CA10–90 reduced by about 10–12% Table 11). The relation between $\eta_c$ and the residual $H_2$ at exhaust differs between the two optimized cases. At HES = 96%, the unburnt $H_2$ mass flow rate is actually slightly lower than in the baseline (−4.4%, Table 12), so that the small reduction in $\eta_c$ (−1.3%) reflects incomplete Diesel oxidation rather than a higher $H_2$ slip, as indicated by the modest rise in unburned hydrocarbons (+11.1 mg/h, Table 12). The behaviour is qualitatively different at HES = 98%: here the strongly reduced Diesel pilot starts to lose efficiency to fully sustain a robust ignition of the ultra-lean $H_2$–air charge, and the unburnt $H_2$ at exhaust increases significantly (+40.8% with respect to the baseline, Table 12), making the drop in $\eta_c$ (−3.2%) clearly attributable to incomplete $H_2$ combustion. The corresponding mechanisms are discussed in detail in the analysis of the in-cylinder $H_2$ mass fraction maps (Fig. 16) presented in the following section.

The behaviour of CO is not monotonic. At HES = 96%, CO emissions are roughly halved (−52%). This indicates that the fraction of Diesel that effectively participates in combustion oxidises very efficiently, with limited CO formation; the small amount of unburnt hydrocarbons (HC) mentioned above corresponds, conversely, to a separate mass of Diesel that survives in locally lean and cooler pockets without entering the combustion process, indicating that Diesel oxidation proceeds relatively close to completion. At HES = 98%, by contrast, the smaller pilot is less effective at driving the final CO-to-$CO_2$ oxidation step to completion, so that CO rises moderately (+60% with respect to the baseline), consistently with the DOE trend in Fig. 11. Combustion nevertheless remains stable. In contrast, the $NO_x$ emissions are drastically reduced in both optimized cases, with reductions of −98.0% at HES = 96% and −99.7% at HES = 98% (Table 12), confirming that ultra-lean, H2-dominated combustion strongly suppresses thermal $NO_x$ formation.

The impact of the optimized injection strategy on in-cylinder pressure and heat release behaviour is illustrated in Fig. 12, which compares the baseline DF configuration with the two optimized cases. In the HES = 96% case, the in-cylinder pressure peak is clearly more pronounced than in the baseline (+31%), and the AHRR exhibits a higher, sharper peak, with the bulk of heat release shifted closer to TDC. In the HES = 98% configuration, the peak pressure is only slightly higher than in the baseline (+5%), while the AHRR becomes flatter and more regular, with a single main peak replacing the pilot–main structure of the original DF case. Overall, both optimized cases show a modified combustion phasing compared with the baseline, while keeping peak $P_{max}$ and PPRR within acceptable mechanical limits and simultaneously achieving very low $NO_x$ and $CO_2$ emissions.

These results confirm that, by properly combining ultra-high HES with a single, strongly advanced Diesel pilot, it is possible to approach an RCCI combustion regime: heat release becomes more homogeneous in the cylinder volume, $CO_2$ and $NO_x$ emissions are drastically reduced,

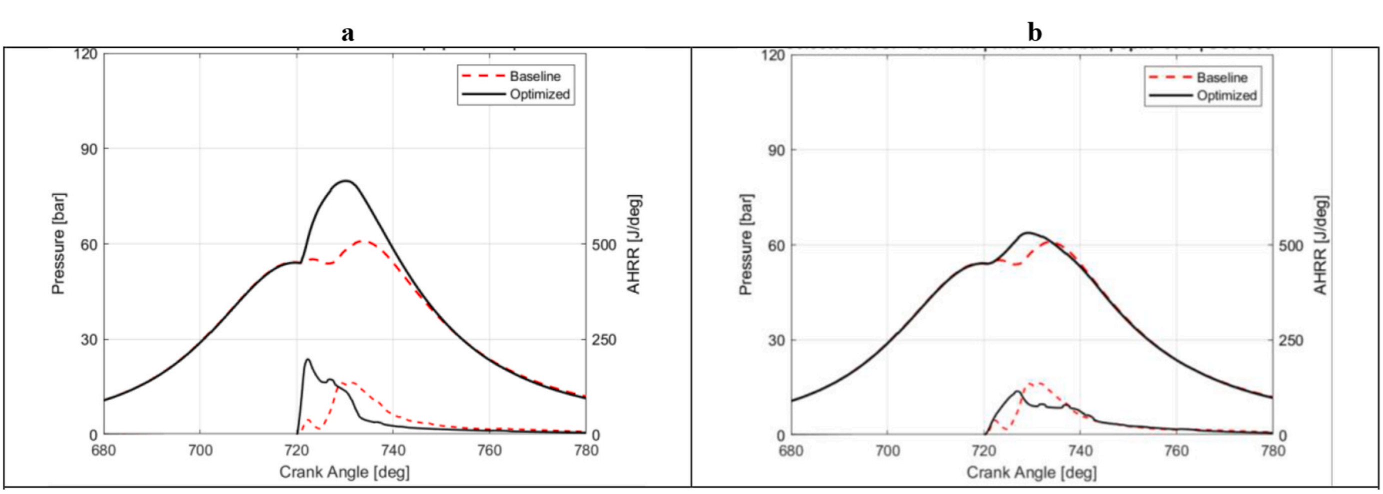


**Fig. 12.** In-cylinder pressure and AHRR comparison between the DF baseline case and the optimized cases: a) HES = 96% pilot SOI = 660°CA, b) HES = 98% pilot SOI 655°CA.

and the engine can still operate with performance comparable to, or even better than, the baseline DF condition.

The mechanical limits adopted as combustion-stability and structural constraints throughout this study (a maximum in-cylinder pressure $P_{max} = 180$ bar and a maximum PPRR = 20 bar/°CA) correspond to the design limits of the research engine, already reported in Table 2. The selection of these two indicators is consistent with the established practice for HD CI and DF engines, in which $P_{max}$ is constrained by the structural integrity of the cranktrain and head gasket, while the PPRR is limited to contain combustion noise and the mechanical load transmitted to the engine structure; an excessive PPRR is indeed recognized as one of the main factors restricting the practical application of DF and RCCI engines at high load [27,57]. The specific PPRR threshold, however, is not universal: it depends on the engine class, its structural robustness and the targeted application, with values around 10 bar/°CA often adopted for light-duty automotive engines [57], whereas more robust HD and research engines can tolerate higher levels. For the large-displacement research engine considered in this study, the structural design limit is PPRR ≤20 bar/°CA, as reported in Table 2. Against these thresholds, the two optimized configurations remain well within the mechanical envelope of the engine. The HES = 96% case reaches $P_{max} = 79.8$ bar and PPRR = 6.28 bar/°CA, while the HES = 98% case reaches $P_{max} = 63.7$ bar and PPRR = 2.57 bar/°CA, against the baseline DF values of 60.9 bar and 1.87 bar/°CA, respectively. Although the advanced single-pilot strategy increases the PPRR with respect to the baseline (by about +237% at HES = 96% and +37% at HES = 98%, owing to the more premixed and energetic auto-ignition of the diesel that promotes $H_2$–air combustion), the resulting values remain far below the 20 bar/°CA structural limit of the present engine, and also below the more conservative 10 bar/°CA threshold typically adopted for light-duty automotive engines, while the corresponding Pmax values stay well below the 180 bar structural threshold. These margins confirm that, at the investigated partial-load condition, the proposed ultra-high HES strategy can be operated with a substantial safety margin against the engine mechanical and NVH limits.

### 3.3. *Mixture formation, in-cylinder temperature fields, and $NO_x$ formation*

The impact of the optimized injection strategy on in-cylinder temperature and $NO_x$ formation is illustrated in Figs. 13 and 14. Fig. 13 compares the crank angle evolution of the mean in-cylinder temperature and the corresponding $NO_x$ formation for the baseline DF configuration and for the two optimized cases. Fig. 14 provides representative temperature contours at selected crank angles for the baseline and the optimized 96% HES case.

For the HES = 96% optimized configuration, the maximum value of the mean in-cylinder temperature slightly increased, as shown in Fig. 13 (a). This might suggest a higher potential for thermal $NO_x$ formation. However, the $NO_x$ trace shows the opposite behaviour: the cumulative $NO_x$ formation trace is drastically reduced compared with the baseline, in line with the integral emission values reported in Table 12. This confirms that thermal $NO_x$ is primarily governed by local temperature peaks rather than by the bulk-averaged temperature.

This mechanism is clarified by the temperature maps in Fig. 14, which show the in-cylinder temperature distribution at four representative crank angles (e.g. 723°, 726°, 730° and 732°CA) for the baseline case (Fig. 14a–d) and for the HES = 96% optimized configuration (Fig. 14e–h). In the baseline DF operation, the main Diesel injection generates well-defined high-temperature regions associated with the diffusion flame, particularly evident around 730–732°CA. These hot spots constitute the primary sites for thermal $NO_x$ formation. In the optimized case, the main injection is removed and the Diesel is injected only as a strongly advanced pilot. The longer premixing time leads to a broader auto-ignition region and a more evenly distributed combustion of the $H_2$–air mixture. As a result, the temperature field becomes significantly more homogeneous.

It is also worth noting that, while local temperatures in the range 1700–1900 K appear in both cases, the regions in which the local temperature exceeds 2000 K (that is, the regime where the thermal $NO_x$ formation rate increases exponentially according to the extended Zeldovich mechanism) are clearly visible only in the baseline DF case. In the optimized HES = 96% configuration these high-temperature regions essentially disappear, and the temperature field remains below the 2000 K threshold throughout the combustion chamber. This suppression of the local peak-temperature regions provides the direct physical mechanism behind the −98% $NO_x$ emission reduction reported in Table 12, consistently with the in-cylinder temperature and $NO_x$ formation traces presented in Fig. 13.

The change in combustion mode is further clarified by the mixture-formation analysis reported in Fig. 15, which shows the spatial distribution of the $C_7H_{16}$ mass fraction in the cylinder charge for the same crank angles as in Fig. 14, with the addition of 718°CA to capture the mixture composition immediately before ignition for both the baseline and the optimized case. In the baseline configuration, the late main injection produces a highly stratified fuel distribution, with dense Diesel-rich regions near the spray axis. These pockets subsequently burn in premixed and then diffusion-controlled conditions, directly giving

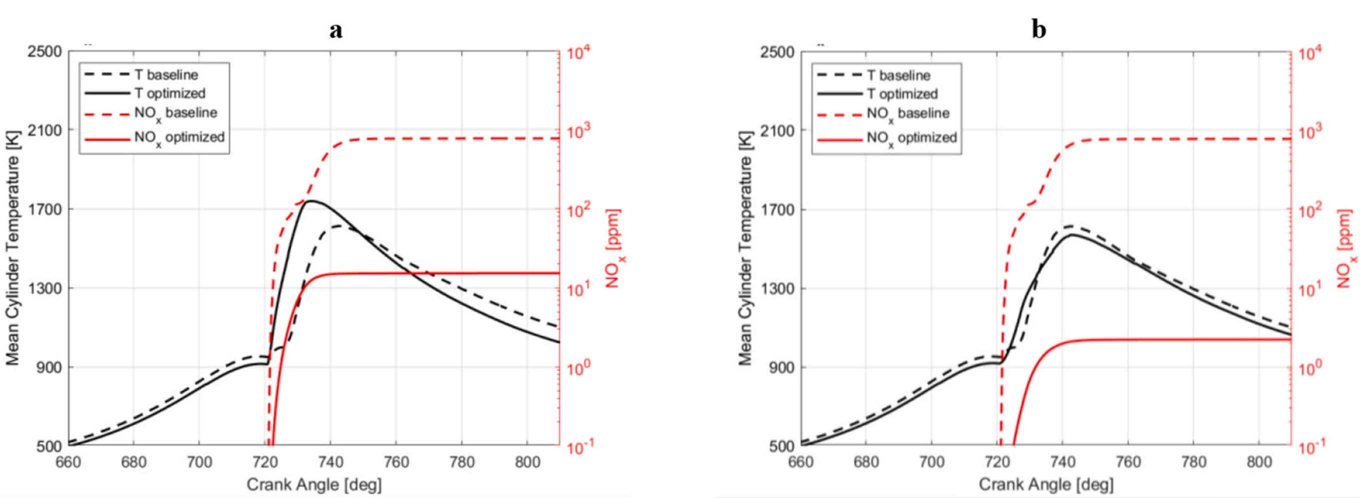


**Fig. 13.** Average in-cylinder temperature and NOx formation plots of the optimized cases, compared with the baseline DF case. a) HES = 96%, pilot SOI = 660°CA, b) HES = 98%, pilot SOI 655°CA.

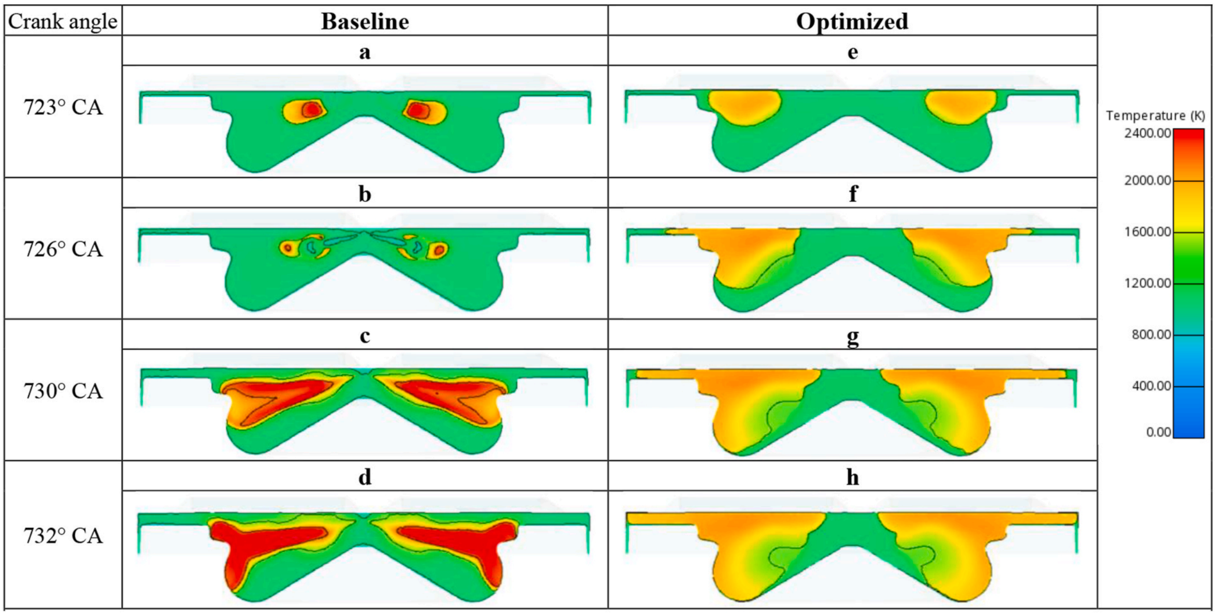


**Fig. 14.** In-cylinder temperature map for baseline DF case (a-d) and optimized HES = 96%, pilot SOI = 660 CA° case (e-h).

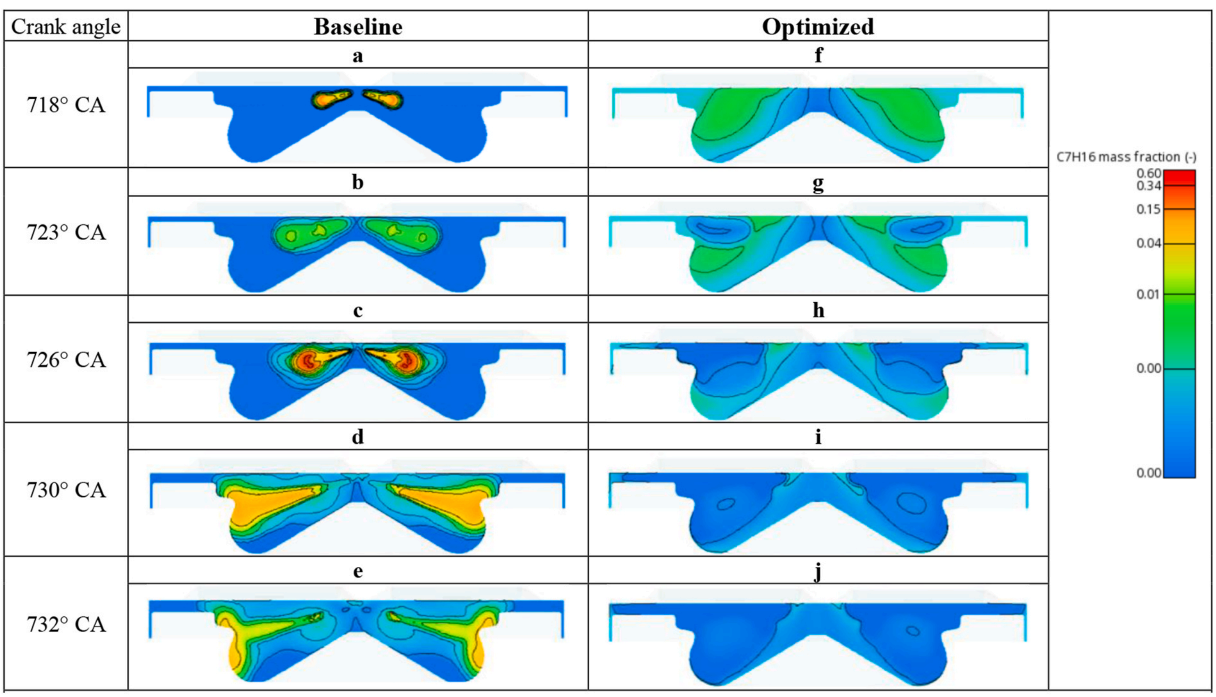


**Fig. 15.** In-cylinder $C_7H_{16}$ mass fraction map for baseline DF case (a-e) and optimized HES = 96%, pilot SOI = 660 CA° case (f-j).

rise to the local temperature. In the optimized HES = 96% case, the early pilot injection has sufficient time to mix with the surrounding charge, and the Diesel-derived mixture appears much more uniformly distributed throughout the chamber. In this configuration, Diesel primarily acts as a distributed ignition promoter for the ultra-lean $H_2$–air mixture, rather than forming localised hot spots.

A similar behaviour is observed for the HES = 98% optimized case (Fig. 13 b). The mean in-cylinder peak temperature is lower but comparable to that of the baseline, whereas $NO_x$ formation remains extremely low over the entire combustion process. Here, the even higher $H_2$ share further strengthens the lean premixed character of the combustion, and the very small Diesel quantity essentially provides ignition without creating hot spots.

These results confirm that the strong $NO_x$ reduction observed in the optimized ultra-high HES cases does not stem from a simple lowering of the overall temperature level, but from a fundamental change in the combustion mode. The transition from a predominant Diesel combustion towards a partially homogeneous, RCCI combustion regime leads to a more evenly distributed heat release, the suppression of local temperature peaks and, consequently, a strong mitigation of thermal $NO_x$ formation, even in the presence of mean temperatures that can exceed those of the baseline DF case.

To quantitatively substantiate the transition from a conventional pilot-ignited DF regime to an RCCI-like combustion mode, the ignition

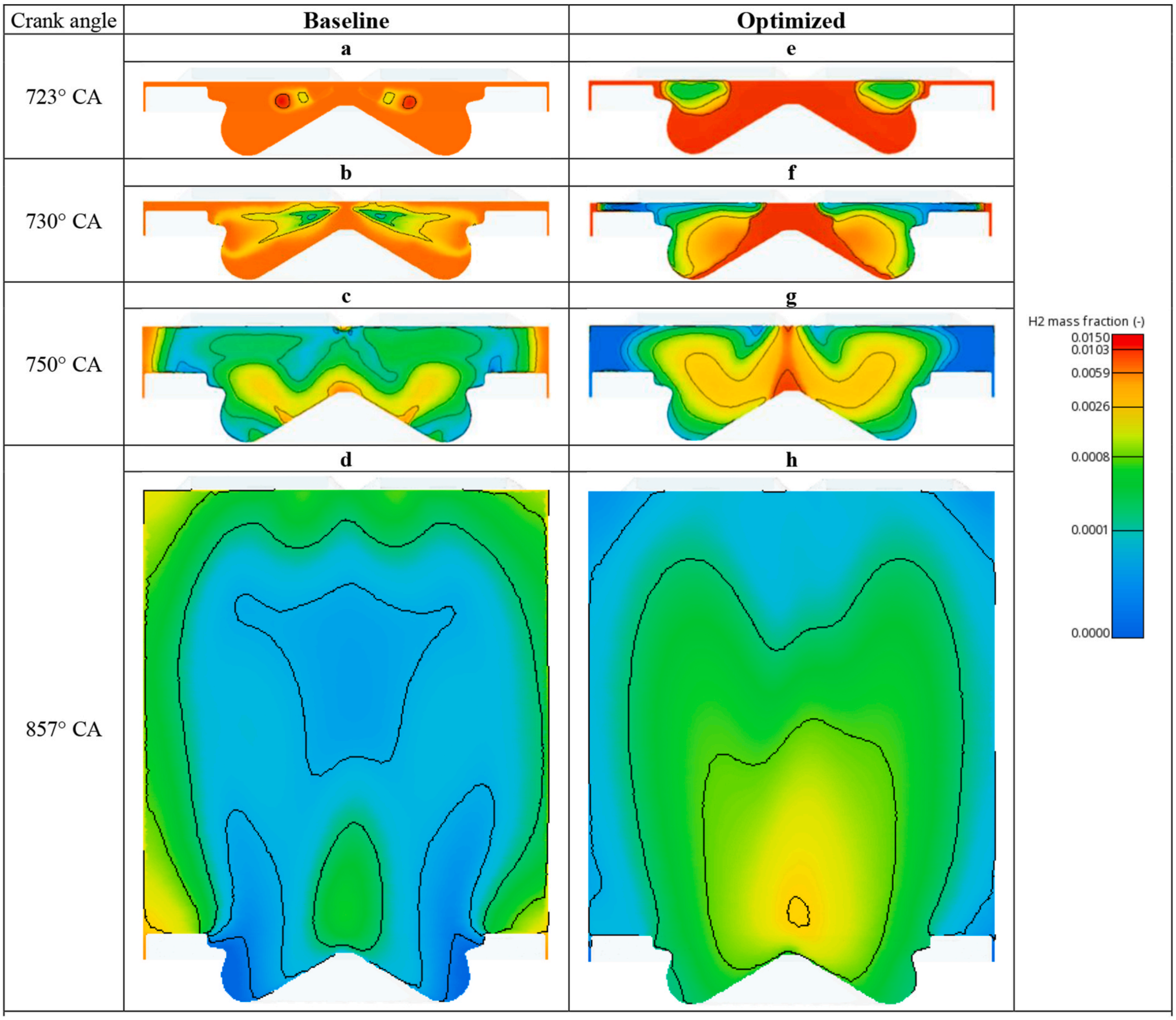


**Fig. 16.** In-cylinder $H_2$ mass fraction map for baseline DF case (a-d) and optimized HES = 96%, pilot SOI = 660 CA° case (e-h).

delay was evaluated for the three cases as the crank-angle interval between the SOI and the CA10. The relevant values are summarized in Table 13. For the baseline DF case, characterised by the conventional pilot-main strategy, the dominant heat-release event is associated to the main injection (SOI = 721.75°CA), which auto-ignites only 6.4°CA later (≈0.9 ms at 1200 rpm). This short delay leaves no significant time for Diesel–air premixing and is consistent with a diffusion-controlled combustion regime, in which the flame propagates from the spray jets. In the optimized cases, the markedly advanced single pilot extends the ignition delay by approximately one order of magnitude, to 62.8°CA at HES = 96% (≈8.7 ms) and 71.0°CA at HES = 98% (≈9.9 ms). Such a long delay allows the Diesel pilot to mix extensively with the ultra-lean $H_2$–air charge and to generate a wider spatially distributed reactivity field.

**Table 13**
Ignition delay metrics for the baseline DF case and the two optimized RCCI configurations.

| Case | SOI | CA 10 | Ignition delay | Ignition delay |
|---|---|---|---|---|
| | (°CA) | (°CA) | (°CA) | (ms) |
| Baseline HES = 67% | 721.75 (main)[a] | 728.2 | 6.5 | 0.9 |
| HES = 96% | 660 (pilot) | 722.8 | 62.8 | 8.7 |
| HES = 98% | 655 (pilot) | 726.0 | 71.0 | 9.9 |

[a] For the baseline DF case, the ignition delay is computed with respect to the main Diesel injection, which is the dominant heat-release event.

To complement the analysis of the in-cylinder temperature and Diesel mass fraction (Figs. 14 and 15), the $H_2$ mass fraction distribution in the cylinder is shown in Fig. 16 at four representative crank-angle stations, for the baseline DF case and the optimized HES = 96% configuration. At 723°CA the baseline shows $H_2$ consumption confined to two small regions in the Diesel pilot jets regions, whereas in the optimized case the $H_2$ consumption is already started and spatially much more diffuse. At 730° and 750°CA the difference becomes more pronounced: in the baseline case the $H_2$ consumption starts from the regions of the Diesel injection, propagating along the injector spray axes, and then progressively reaches the peripheral regions of the chamber, so that at 750°CA a small portion of the squish region close to the cylinder liner and the crevice areas have not yet been involved in the combustion; in the optimized case, conversely, the $H_2$ has already been consumed almost completely in the upper bowl and squish regions, while a central $H_2$-richer pocket starts to form in the middle of the bowl and around the cylinder axis. At 857°CA (EVO) the contrast between the two cases becomes evident and is the direct consequence of the different propagation paths observed during the combustion phase. In the baseline case the residual $H_2$ is distributed in the outer regions of the cylinder and in the piston-liner crevices, consistently with the late involvement of these peripheral zones in the flame propagation; in the optimized case, on the contrary, the residual $H_2$ is mostly concentrated in a well-defined central pocket expanding from the middle of the bowl, which is the direct evolution of the central $H_2$-rich region already visible at 730° and 750°CA.

The spatial coincidence between this residual $H_2$ pocket and the region of minimum Diesel penetration visible in Fig. 15 indicates that, with the markedly advanced single-pilot strategy, the bowl-shaped combustion chamber and the injector spray cone (both originally designed for conventional pilot-ignited Diesel) leave the central region of the bowl essentially unreached by the high-reactivity fuel. As a consequence, the lean $H_2$–air charge in this region lacks a local ignition source and for this reason $H_2$ remains partially unburned.

Quantitatively, the fraction of $H_2$ remaining unburned at EVO with respect to the $H_2$ trapped at IVC is 4.55% for the baseline DF case, 3.02% for the HES = 96% optimized case and 4.38% for the HES = 98% optimized case. In absolute terms, the optimized HES = 96% case actually emits slightly less unburned $H_2$ than the baseline (26.0 vs 27.2 g/h, i.e. about 1.2 g/h less). The corresponding combustion efficiency is only marginally lower than the baseline (0.94 vs 0.96 see Table 11), the slight reduction being attributable to a small fraction of chemical energy that remains bound in incomplete Diesel oxidation path in the absence of the locally high-temperature pockets typical of Diesel diffusive combustion. This is consistent with the modest increase observed for unburned hydrocarbons (+33% with respect to baseline), which mark the survival of small amounts of Diesel pilot in locally lean pockets; from a practical standpoint, this residual fraction can be effectively addressed by conventional oxidation aftertreatment downstream of the cylinder.

Overall, the observed phenomena suggest that the combustion-chamber geometry and the injector configuration adopted in the present study (designed for conventional Diesel and DF operation) are not optimally suited to a single-pilot RCCI strategy with strongly advanced injection. A natural direction for future work is the redesign of the bowl shape and the optimization of the injector spray-cone angle to redistribute the Diesel pilot also towards the central region of the bowl, thereby reducing the formation of the residual $H_2$ pocket at the source.

For the HES = 98% configuration the picture is qualitatively similar but less favourable: the further reduction of the Diesel pilot leaves a larger portion of the bowl core without a local ignition source, so that the central unburned-$H_2$ pocket grows. The unburned-$H_2$ fraction at EVO rises to 4.38% (a +40.8% increase in unburned-$H_2$ mass flow with respect to the baseline) and CO increases moderately (+60%), indicating that the reduced Diesel quantity is less effective at driving the charge oxidation to completion. Combustion nevertheless remains stable, so that HES = 98% can be regarded as the practical upper limit of the proposed strategy rather than a failure point.

In this framework, the HES = 96% optimized configuration is particularly attractive, as it combines a manageable increase in $P_{max}$ with a gain in GIE and reduced carbon-based emissions. It should be emphasized that the present investigation is carried out on a large single-cylinder research engine, and that the proposed ultra-high HES DF strategy is not tailored to a specific final application, but is instead representative of a generic HD use that could be adapted to different sectors (on-road, off-road, marine, etc.). Nevertheless, it is instructive to benchmark the achieved $NO_x$ levels against the Euro 7 law emission limits for on-road engines, purely as an illustrative reference. To this end, a dedicated comparison is reported in Table 14, which shows that, under the investigated low-load and ultra-high HES conditions, the optimized HES = 96% case attains $NO_x$ levels of the order of half the Euro 7 threshold. This benchmark highlights that, despite the research-oriented nature of the analysis, the proposed combustion strategy can already be regarded as a low emission mode in terms of both carbon-based species and $NO_x$.

**Table 14**
Optimized HES = 96%, pilot SOI = 660°CA case vs Euro 7 comparison in terms of NOx emissions.

| | Opt. HES = 96% | Euro 7 limit | |
|---|---|---|---|
| | | Test bench | RDE |
| **$NO_x$ (mg/kWh)** | 115 | 200 | 260 |

## 4. Conclusions

In this work, an experimentally calibrated 3D-CFD model has been used to numerically investigate the feasibility of ultra-high HES D–$H_2$ DF operation under a representative low-load condition (1200 rpm, IMEP = 6 bar). The study is conceived as a conceptual numerical demonstration at low load, intended to delineate the achievable combustion behaviour, the associated mechanical and emission trade-offs, and the practical limits of a single-pilot RCCI strategy in a HD CI architecture.

The main outcomes of the present investigation are summarized below.

- The 3D-CFD model has been calibrated and validated against nine experimental operating points spanning three loads (IMEP = 6, 12 and 18 bar) and three global excess-air ratios ($\lambda_g$), using a single common set of combustion-model parameters and providing an internally consistent baseline for the subsequent optimization campaign.
- Starting from a partial-load DF baseline (IMEP = 6 bar, $\lambda_g \approx 2.56$, HES = 67%), a DOE on the Diesel pilot SOI (SOI) has been carried out at three ultra-high HES levels (96%, 98% and 99%). Stable combustion has been obtained up to HES ≈96–98% within a limited SOI window, whereas at HES = 99% the strongly reduced Diesel quantity is no longer sufficient to guarantee a robust ignition for any of the tested timings.
- Two optimized configurations have been identified: HES = 96% with SOI = 660°CA and HES = 98% with SOI = 655°CA. With respect to the DF baseline, the HES = 96% case delivers +4.4% GIE, −88.6% $CO_2$ and −98% $NO_x$ emissions; the HES = 98% case further reduces $CO_2$ by 94% and $NO_x$ by 99.7%, at the cost of a moderate GIE penalty and higher unburned $H_2$ at the exhaust for the higher HES case (+40.8% with respect to the baseline).
- In both optimized cases, the PPRR remains within the mechanical limit of the engine (20 bar/°CA) and the peak in-cylinder pressure stays below the design threshold of 180 bar, confirming the structural feasibility of the strategy at the investigated operating point.
- The analysis of the in-cylinder fields clarifies the physical origin of the $NO_x$ reduction: although bulk-averaged temperatures are comparable to the baseline, the local high-temperature pockets associated with Diesel diffusion combustion are largely suppressed in the optimized cases, owing to the markedly advanced pilot SOI that promotes a more homogeneous mixture and a spatially distributed ignition process, consistent with an RCCI-like combustion regime.
- When benchmarked against the Euro 7 $NO_x$ thresholds for on-road vehicles, the optimized operating points lie well below the regulatory limit, with predicted $NO_x$ of the order of half the threshold.

The interpretation of the present results must be framed within the limitations of the modelling approach adopted. The optimized HES = 96% and HES = 98% configurations have not been experimentally validated and rely on the predictive capability of the 3D-CFD model beyond the calibration matrix; the absolute emission levels should therefore be regarded as indicative, and the analysis is most robust when interpreted in terms of relative trends with respect to the DF baseline rather than in terms of absolute values. The emission model itself was calibrated against the experimental data through constant multiplicative correction factors, so that its reliability is well established within the validated operating range. The assessment has moreover been carried out under steady-state, closed-valve conditions with a homogeneous

$H_2$–air mixture at IVC, so that transients, cycle-to-cycle variability and intake/exhaust gas-exchange effects are not captured. These limitations also delimit the regulatory implications of the benchmarking against the Euro 7 thresholds, which should be read in relative rather than absolute terms.

The main result of the present study is the numerical demonstration that, under representative low-load conditions and within a calibrated 3D-CFD framework, a single, markedly advanced Diesel pilot can drive a RCCI regime extending the HES up to 98% without recourse to dual-pulse injection, EGR or water injection, while preserving GIE, containing $P_{max}$ and PPRR within the engine mechanical envelope, and substantially reducing both carbon-based and $NO_x$ emissions with respect to the DF baseline.

On this basis, the following directions for future work are recommended.

- Experimental validation of the predicted ultra-high HES configurations on the same test bench, providing measured pressure traces, $NO_x$ and unburned $H_2$ levels at the optimized operating points, to confirm the predictive capability of the 3D-CFD model in the extrapolation region;
- Extension of the strategy to medium and high loads, where the faster heat release associated with ultra-high HES is expected to require additional control levers (Variable Valve Actuation for effective compression-ratio reduction, increased dilution, water injection or optimized split injections) to contain $P_{max}$ and PPRR within the mechanical envelope;
- Assessment of the robustness of the optimized strategy under transient and cycle-to-cycle variability, complementing the steady-state analysis presented in this work;
- Redesign of the piston-bowl geometry and of the injector spray-cone angle to better suit the single-pilot RCCI strategy; directing the high-reactivity pilot toward the central region of the chamber is expected to suppress the central unburned-$H_2$ pocket identified in this work, thereby further improving combustion efficiency and reducing unburned $H_2$.
- Assessment of dedicated aftertreatment solution for residual $H_2$ oxidation, in view of practical deployment.

In closing, the present numerical investigation contributes to the broader perspective of retrofitting the existing HD CI installed base, across road, off-road and marine sectors, toward Diesel–$H_2$ DF operation as a transitional pathway to decarbonisation. The results obtained at low load indicate that, even within the constraints of an unmodified engine architecture, a careful reorientation of the Diesel injection strategy alone is sufficient to extend the HES to ultra-high values, while preserving thermodynamic efficiency and respecting the mechanical envelope of the engine. The extension of this approach to medium and high loads, which is essential to make Diesel–$H_2$ retrofit a credible decarbonisation lever for real-world HD duty cycles, emerges as the natural next research priority.

## CRediT authorship contribution statement

**Alfredo Maria Pisapia:** Conceptualization, Data curation, Formal analysis, Investigation, Methodology, Resources, Software, Validation, Visualization, Writing – original draft, Writing – review & editing. **Carlo Alberto Rinaldini:** Conceptualization, Data curation, Formal analysis, Investigation, Methodology, Resources, Software, Supervision, Validation, Visualization, Writing – original draft, Writing – review & editing. **Francesco Scrignoli:** Conceptualization, Data curation, Formal analysis, Investigation, Methodology, Resources, Software, Validation, Visualization, Writing – original draft, Writing – review & editing. **Xinyan Wang:** Conceptualization, Data curation, Formal analysis, Investigation, Methodology, Resources, Software, Supervision, Validation, Visualization, Writing – original draft, Writing – review & editing. **Hua Zhao:** Conceptualization, Data curation, Formal analysis, Investigation, Methodology, Resources, Software, Supervision, Validation, Visualization, Writing – original draft, Writing – review & editing.

## Declaration of competing interest

The authors declare that they have no known competing financial interests or personal relationships that could have appeared to influence the work reported in this paper.

## Acknowledgments

AVL Italia Srl and AVL List GmbH is the company providing the software. The authors would like to thank AVL Italia Srl and AVL List GmbH for the FIRE M 2023.2 license granted to the University of Modena and Reggio Emiliais the beneficiary.

## Appendix A

**Table A1**
Measurement equipment used in the experimental campaign, with the corresponding device, manufacturer, measurement range, and linearity/accuracy.

| Measurement | Device | Manufacturer | Measurement range | Linearity/Accuracy |
|---|---|---|---|---|
| Engine speed | AG 150 dynamometer | Froude Hofmann | 0-8000 rpm | ±1 rpm |
| Engine torque | AG 150 dynamometer | Froude Hofmann | 0-500 Nm | ±0.25% of FS |
| Clock Signal | EB58 | Encoder Technology | 0-25000 rpm | 0.25 CAD |
| Diesel flow rate (supply) | Proline Promass 83A02 | Endress + Hauser | 0-20 kg/h | ±0.10% of reading |
| Diesel flow rate (return) | Proline Promass 83A01 | Endress + Hauser | 0-100 kg/h | ±0.10% of reading |
| Hythane flow rate | Proline Promass 80A02 | Endress + Hauser | 0-20 kg/h | ±0.15% of reading |
| Hydrogen flow rate | Coriolis flowmeter K000000453 | Alicat Scientific | 0-10 kg/h | ±0.20% of reading |
| Intake air mass flow rate | Proline T-mass 65F | Endress + Hauser | 0-910 kg/h | ±1.5% of reading |
| In-cylinder pressure | Piezoelectric pressure sensor Type 6125C | Kistler | 0-30 MPa | ≤ ±0.4% of FS |
| Intake and exhaust pressures | Piezoresistive pressure sensor Type 4049A | Kistler | 0-1 MPa | ≤ ±0.5% of FS |
| Oil pressure | Pressure transducer UNIK 5000 | GE | 0-1 MPa | < ±0.2% of FS |
| Temperature | Thermocouple K Type | RS | 233-1473 K | ≤ ±2.5 K |
| Fuel injector current signal | Current probe PR30 | LEM | 0-20 A | ±2 mA |
| Smoke number | 415SE | AVL | 0-10 FSN | - |

(*continued on next page*)

**Table A1** (*continued*)

| Measurement | Device | Manufacturer | Measurement range | Linearity/Accuracy |
|---|---|---|---|---|
| CO emission | MEXA-7170-DEGR (Non-Dispersive Infrared Detector) | Horiba | 0-12 vol% | ≤ ±1.0% of FS or ±2.0% of readings |
| $CO_2$ emission | MEXA-7170-DEGR (Non-Dispersive Infrared Detector) | Horiba | 0-20 vol% | ≤ ±1.0% of FS or ±2.0% of readings |
| THC emission | MEXA-7170-DEGR (Heated Flame Ionization Detector) | Horiba | 0-500 ppm or 0-50k ppm | ≤ ±1.0% of FS or ±2.0% of readings |
| $CH_4$ emission | MEXA-7170-DEGR (Non-Methane Cutter + Heated Flame Ionization Detector) | Horiba | 0-0.25k ppm or 0-25k ppm | ≤ ±1.0% of FS or ±2.0% of readings |
| NO/NOx emission | MEXA-7170-DEGR (Heated Chemiluminescence Detector) | Horiba | 0-500 ppm or 0-10k ppm | ≤ ±1.0% of FS or ±2.0% of readings |
| Hydrogen emissions | Air sens500 | V&F | 0-5000 ppm or 0-100% vol | 0.5% of fs or 1%vol |

## References


[1] Climate change - NASA science. https://science.nasa.gov/climate-change/. [Accessed 16 December 2025].
[2] Climate change: global temperature | NOAA Climate.gov. https://www.climate.gov/news-features/understanding-climate/climate-change-global-temperature. [Accessed 16 December 2025].
[3] Hertzberg M, Siddons A, Schreuder H. Role of greenhouse gases in climate change. Energy Environ 2017;28:530–9. https://doi.org/10.1177/0958305X17706177.
[4] COP28. Consilium n.d. https://www.consilium.europa.eu/en/policies/paris-agreement-climate/cop28/(accessed December 16, 2025).
[5] Qazi S, Venugopal P, Rietveld G, Soeiro TB, Shipurkar U, Grasman A, et al. Powering maritime: challenges and prospects in ship electrification. IEEE Electrif Mag 2023;11:74–87. https://doi.org/10.1109/MELE.2023.3264926.
[6] Un-Noor F, Wu G, Perugu H, Collier S, Yoon S, Barth M, et al. Off-Road construction and agricultural equipment electrification: review, challenges, and opportunities. Vehicles 2022;4:780–807. https://doi.org/10.3390/vehicles4030044.
[7] Gross S. The challenge of decarbonizing heavy transport. 2020.
[8] Kolahchian Tabrizi M, Cerri T, Bonalumi D, Lucchini T, Brenna M. Retrofit of diesel engines with H2 for potential decarbonization of non-electrified railways: assessment with lifecycle analysis and advanced numerical modeling. Energies 2024;17:996. https://doi.org/10.3390/en17050996.
[9] European Commission. Joint Research Centre. Decarbonisation of heavy duty vehicle transport: zero emission heavy goods vehicles : workshop summary report (28 October 2020, JRC Petten, Netherlands). LU. Publications Office; 2021.
[10] Karystinos V, Papalambrou G. Retrofit, experimental, and Numerical evaluation of a high-speed diesel engine for diesel-methanol dual-fuel operation. J Eng Gas Turbines Power 2025;147:101019. https://doi.org/10.1115/1.4068944.
[11] Hosseini SH, Tsolakis A, Alagumalai A, Mahian O, Lam SS, Pan J, et al. Use of hydrogen in dual-fuel diesel engines. Prog Energy Combust Sci 2023;98:101100. https://doi.org/10.1016/j.pecs.2023.101100.
[12] Saravanan N, Nagarajan G. Performance and emission studies on port injection of hydrogen with varied flow rates with Diesel as an ignition source. Appl Energy 2010;87:2218–29. https://doi.org/10.1016/j.apenergy.2010.01.014.
[13] Mancaruso E, Robbio RD, Vaglieco BM. Hydrogen/Diesel combustion analysis in a single cylinder research engine. SAE Int J Adv & Curr Prac in Mobility 2022;5: 1312–21. https://doi.org/10.4271/2022-24-0012.
[14] Mancaruso E, Rossetti S, Vaglieco BM, Robbio RD, Maroteaux F. Optical diagnostics to Study Hydrogen/Diesel combustion with EGR in a single cylinder research engine. SAE Technical Paper 2023. https://doi.org/10.4271/2023-24-0070.
[15] Saravanan N, Nagarajan G. An experimental investigation on optimized manifold injection in a direct-injection diesel engine with various hydrogen flowrates. Proc Inst Mech Eng - Part D J Automob Eng 2007;221:1575–84. https://doi.org/10.1243/09544070JAUTO609.
[16] Sharma P, Dhar A. Effect of hydrogen fumigation on combustion stability and unregulated emissions in a diesel fuelled compression ignition engine. Appl Energy 2019;253:113620. https://doi.org/10.1016/j.apenergy.2019.113620.
[17] Şanlı A, Yılmaz İT. Cycle-to-cycle combustion analysis in hydrogen fumigated common-rail diesel engine. Fuel 2022;320:123887. https://doi.org/10.1016/j.fuel.2022.123887.
[18] Varde K, Frame G. Hydrogen aspiration in a direct injection type diesel engine-its effects on smoke and other engine performance parameters. Int J Hydrogen Energy 1983;8:549–55. https://doi.org/10.1016/0360-3199(83)90007-1.
[19] Nag S, Sharma P, Gupta A, Dhar A. Experimental study of engine performance and emissions for hydrogen diesel dual fuel engine with exhaust gas recirculation. Int J Hydrogen Energy 2019;44:12163–75. https://doi.org/10.1016/j.ijhydene.2019.03.120.
[20] Saravanan N, Nagarajan G. An experimental investigation of hydrogen-enriched air induction in a diesel engine system. Int J Hydrogen Energy 2008;33:1769–75. https://doi.org/10.1016/j.ijhydene.2007.12.065.
[21] Chintala V, Subramanian KA. Experimental investigations on effect of different compression ratios on enhancement of maximum hydrogen energy share in a compression ignition engine under dual-fuel mode. Energy 2015;87:448–62. https://doi.org/10.1016/j.energy.2015.05.014.
[22] Lata DB, Misra A, Medhekar S. Investigations on the combustion parameters of a dual fuel diesel engine with hydrogen and LPG as secondary fuels. Int J Hydrogen Energy 2011;36:13808–19. https://doi.org/10.1016/j.ijhydene.2011.07.142.
[23] Lilik GK, Zhang H, Herreros JM, Haworth DC, Boehman AL. Hydrogen assisted diesel combustion. Int J Hydrogen Energy 2010;35:4382–98. https://doi.org/10.1016/j.ijhydene.2010.01.105.
[24] Cho Y, Song S, Chun KM. H2 effects on diesel combustion and emissions with an LPL-EGR system. Int J Hydrogen Energy 2013;38:9897–906. https://doi.org/10.1016/j.ijhydene.2013.05.143.
[25] Sandalcı T, Karagöz Y. Experimental investigation of the combustion characteristics, emissions and performance of hydrogen port fuel injection in a diesel engine. Int J Hydrogen Energy 2014;39:18480–9. https://doi.org/10.1016/j.ijhydene.2014.09.044.
[26] Talibi M, Hellier P, Ladommatos N. The effect of varying EGR and intake air boost on hydrogen-diesel co-combustion in CI engines. Int J Hydrogen Energy 2017;42: 6369–83. https://doi.org/10.1016/j.ijhydene.2016.11.207.
[27] Reitz RD, Duraisamy G. Review of high efficiency and clean reactivity controlled compression ignition (RCCI) combustion in internal combustion engines. Prog Energy Combust Sci 2015;46:12–71. https://doi.org/10.1016/j.pecs.2014.05.003.
[28] Kokjohn SL, Hanson RM, Splitter DA, Reitz RD. Fuel reactivity controlled compression ignition (RCCI): a pathway to controlled high-efficiency clean combustion. Int J Engine Res 2011;12:209–26. https://doi.org/10.1177/1468087411401548.
[29] Paykani A, Kakaee A-H, Rahnama P, Reitz RD. Effects of diesel injection strategy on natural gas/diesel reactivity controlled compression ignition combustion. Energy 2015;90:814–26. https://doi.org/10.1016/j.energy.2015.07.112.
[30] Saravanan N, Nagarajan G. An experimental investigation on manifold-injected hydrogen as a dual fuel for diesel engine system with different injection duration. Int J Energy Res 2009;33:1352–66. https://doi.org/10.1002/er.1550.
[31] Tomita E, Kawahara N, Piao Z, Fujita S, Hamamoto Y. Hydrogen combustion and exhaust emissions ignited with diesel oil in a dual fuel engine. 2001-01–3503, https://doi.org/10.4271/2001-01-3503; 2001.
[32] Rameez PV, Mohamed Ibrahim M. Maximizing hydrogen utilization in CI engines: an investigation of dual fuel and RCCI combustion approaches under low and mid-load conditions in a medium duty automotive engine. Energy Convers Manag 2024;321:119100. https://doi.org/10.1016/j.enconman.2024.119100.
[33] Dimitriou P, Kumar M, Tsujimura T, Suzuki Y. Combustion and emission characteristics of a hydrogen-diesel dual-fuel engine. Int J Hydrogen Energy 2018; 43:13605–17. https://doi.org/10.1016/j.ijhydene.2018.05.062.
[34] De Morais AM, Mendes Justino MA, Valente OS, Hanriot SDM, Sodré JR. Hydrogen impacts on performance and CO2 emissions from a diesel power generator. Int J Hydrogen Energy 2013;38:6857–64. https://doi.org/10.1016/j.ijhydene.2013.03.119.
[35] Bose PK, Deb M, Banerjee R, Majumder A. Multi objective optimization of performance parameters of a single cylinder diesel engine running with hydrogen using a Taguchi-fuzzy based approach. Energy 2013;63:375–86. https://doi.org/10.1016/j.energy.2013.10.045.
[36] Nguyen TA, Mikami M. Effect of hydrogen addition to intake air on combustion noise from a diesel engine. Int J Hydrogen Energy 2013;38:4153–62. https://doi.org/10.1016/j.ijhydene.2013.01.082.
[37] Schwoerer JA, Kumar K, Ruggiero B, Swanbon B. Lost-Motion VVA systems for enabling next generation diesel engine efficiency and after-treatment optimization, Detroit. United States: Michigan; 2010. https://doi.org/10.4271/2010-01-1189. 2010-01–1189.
[38] Dittrich PA, Peter F, Huber G, Kuehn M. Thermodynamic potentials of a fully variable valve actuation System for passenger-car diesel engines. SAE International 2010. https://doi.org/10.4271/2010-01-1199.
[39] AVL FIRE M 2023 R2, AVL List, Graz, Austria. 2023.
[40] Fridriksson H, Sunden B, Hajireza S, Tuner M. CFD investigation of heat transfer in a diesel engine with diesel and PPC combustion modes. Japan: Kyoto; 2011. https://doi.org/10.4271/2011-01-1838. 2011-01–1838.
[41] Millo F, Piano A, Roggio S, Pastor JV, Micó C, Lewiski F, et al. Mixture formation and combustion process analysis of an innovative diesel piston bowl design

through the synergetic application of numerical and optical techniques. Fuel 2022; 309:122144. https://doi.org/10.1016/j.fuel.2021.122144.
[42] Scrignoli F, Pisapia AM, Savioli T, Mancaruso E, Mattarelli E, Rinaldini CA. Exploring hydrogen–diesel dual fuel combustion in a light-duty engine: a numerical investigation. Energies 2024;17:5761. https://doi.org/10.3390/en17225761.
[43] Hanjalić K, Popovac M, Hadžiabdić M. A robust near-wall elliptic-relaxation eddy-viscosity turbulence model for CFD. Int J Heat Fluid Flow 2004;25:1047–51. https://doi.org/10.1016/j.ijheatfluidflow.2004.07.005.
[44] Durbin PA. Near-wall turbulence closure modeling without "damping functions.". Theor Comput Fluid Dynam 1991;3:1–13. https://doi.org/10.1007/BF00271513.
[45] Tatschl R. Diesel spray modeling including multidimensional cavitating nozzle flow effects. Proc ILASS-Europe 2000 2000.
[46] Künsberg-Sarre C, Tatschl R. Spray Modeling/Atomisation-Current status of Break-up models. IMECHE-Seminar; December, 1998. p. 15–6.
[47] Pham VC, Choi J-H, Rho B-S, Kim J-S, Park K, Park S-K, et al. A numerical Study on the combustion process and emission characteristics of a natural gas-diesel dual-fuel marine engine at full load. Energies 2021;14:1342. https://doi.org/10.3390/en14051342.
[48] Luo J, Liu Z, Wang J, Chen H, Zhang Z, Qin B, et al. Effects of different injection strategies on combustion and emission characteristics of diesel engine fueled with dual fuel. Processes 2021;9:1300. https://doi.org/10.3390/pr9081300.
[49] Colin O, Benkenida A. The 3-Zones extended coherent flame model (Ecfm3z) for computing Premixed/Diffusion combustion. Oil & Gas Science and Technology - Rev IFP 2004;59:593–609. https://doi.org/10.2516/ogst:2004043.
[50] Anetor L, Odetunde C, Osakue EE. Computational analysis of the extended zeldovich mechanism. Arabian J Sci Eng 2014;39:8287–305. https://doi.org/10.1007/s13369-014-1398-7.
[51] Senecal PK, Pomraning E, Richards KJ, Briggs TE, Choi CY, McDavid RM, et al. Multi-Dimensional modeling of direct-injection diesel spray liquid length and Flam lift-off length using CFD an parallel detailed Chemistry n.d.
[52] Ferrari G, Onorati A, D'Errico G. Internal combustion engines. Società Editrice Esculapio 2022.
[53] Goyal H, Jones P, Bajwa A, Parsons D, Akehurst S, Davy MH, et al. Design trends and challenges in hydrogen direct injection (H2DI) internal combustion engines – a review. Int J Hydrogen Energy 2024;86:1179–94. https://doi.org/10.1016/j.ijhydene.2024.08.284.
[54] Musy F, Ortiz R, Ortiz I, Ortiz A. Hydrogen-fuelled internal combustion engines: direct Injection versus Port-Fuel Injection. Int J Hydrogen Energy 2025;137: 925–38. https://doi.org/10.1016/j.ijhydene.2024.07.136.
[55] Fayaz H, Saidur R, Razali N, Anuar FS, Saleman AR, Islam MR. An overview of hydrogen as a vehicle fuel. Renew Sustain Energy Rev 2012;16:5511–28. https://doi.org/10.1016/j.rser.2012.06.012.
[56] Stępień Z. A comprehensive overview of hydrogen-fueled internal combustion engines: achievements and future challenges. Energies 2021;14. https://doi.org/10.3390/en14206504.
[57] Chu S, Lee J, Kang J, Lee Y, Min K. High load expansion with low emissions and the pressure rise rate by dual-fuel combustion. Appl Therm Eng 2018;144:437–43. https://doi.org/10.1016/j.applthermaleng.2018.08.027.